The Astrophysical Journal, 803:23 (24pp), 2015 April 10 doi:10.1088/0004-637X/803/1/23

CO-SPATIAL LONG-SLIT UV/OPTICAL SPECTRA OF 10 GALACTIC PLANETARY NEBULAE WITH *HST*/STIS. I. DESCRIPTION OF THE OBSERVATIONS, GLOBAL EMISSION-LINE MEASUREMENTS, AND CNO ABUNDANCES*

Reginald J. Dufour[1], Karen B. Kwitter[2], Richard A. Shaw[3], Richard B. C. Henry[4], Bruce Balick[5], and Romano L. M. Corradi[6,7]
[1] Department of Space Physics and Astronomy, Rice University, Houston, TX 77251, USA
[2] Department of Astronomy, Williams College, Williamstown, MA 01267, USA
[3] National Optical Astronomy Observatory, Tucson, AZ 85719, USA
[4] Department of Physics and Astronomy, University of Oklahoma, Norman, OK 73019, USA
[5] Department of Astronomy, University of Washington, Seattle, WA 98195, USA
[6] Instituto de Astrofísica de Canarias, E-38200 La Laguna, Tenerife, Spain
[7] Departamento de Astrofísica, Universidad de La Laguna, E-38206 La Laguna, Tenerife, Spain
Received 2014 November 18; accepted 2015 February 12; published 2015 April 9

ABSTRACT

We present observations and initial analysis from a *Hubble Space Telescope* (*HST*) Cycle 19 program using STIS to obtain the first co-spatial, UV–optical spectra of 10 Galactic planetary nebulae (PNs). Our primary objective was to measure the critical emission lines of carbon and nitrogen with unprecedented signal-to-noise ratio (S/N) and spatial resolution over the wavelength range 1150–10270 Å, with the ultimate goal of quantifying the production of these elements in low- and intermediate-mass stars. Our sample was selected from PNs with a near-solar metallicity, but spanning a broad range in N/O based on published ground-based and *IUE* spectra. This study, the first of a series, concentrates on the observations and emission-line measurements obtained by integrating along the entire spatial extent of the slit. We derived ionic and total elemental abundances for the seven PNs with the strongest UV line detections (IC 2165, IC 3568, NGC 2440, NGC 3242, NGC 5315, NGC 5882, and NGC 7662). We compare these new results with other recent studies of the nebulae and discuss the relative merits of deriving the total elemental abundances of C, N, and O using ionization correction factors (ICFs) versus summed abundances. For the seven PNs with the best UV line detections, we conclude that summed abundances from direct diagnostics of ions with measurable UV lines give the most accurate values for the total elemental abundances of C and N (although ICF abundances often produced good results for C). In some cases where significant discrepancies exist between our abundances and those from other studies, we show that the differences can often be attributed to their use of fluxes that are not co-spatial. Finally, we examined C/O and N/O versus O/H and He/H in well-observed Galactic, LMC, and SMC PNs and found that highly accurate abundances are essential for properly inferring elemental yields from their progenitor stars. Future papers will discuss photoionization modeling of our observations, of both the integrated spectra and spatial variations of the UV versus optical lines along the STIS slit lengths, which are unique to our observations.

Key words: galaxies: evolution – ISM: abundances – planetary nebulae: general – stars: evolution

1. INTRODUCTION

The elements carbon (C) and nitrogen (N) are present in all known life forms, and identifying the major stellar production sources of these elements is one of the most pressing problems in galactic abundance and astrobiology studies today. That C and N are synthesized and ejected by both massive stars and low- and intermediate-mass stars ($0.8\,M_{\odot} \leqslant M \leqslant 8\,M_{\odot}$; LIMSs) is not in doubt. The existence in the Galaxy of WC and WN stars with progenitor masses exceeding $20\,M_{\odot}$, as well as carbon stars and planetary nebulae (PNs) with LIMS as progenitors, suggests that the Galactic level of these elements is likely mediated by both components of the mass spectrum. The real challenge is to determine the proportional contribution that each component makes.

Numerous theorists have used stellar evolution models to predict the fraction of synthesized C and N, as a function of progenitor mass and metallicity, that LIMS eject into their PNs. Historically, optical spectra of collisionally excited emission lines in PNs have been used to determine N and O abundances from the strong emission lines of [O II] λ3727, [O III] $\lambda\lambda$4959, 5007, and [N II] $\lambda\lambda$6548, 6583. However, in a majority of PNs N^{+} represents only a very minor fraction of the total N abundance, and the ratio of O^{+}/O^{++} has been used as an ionization correction factor (ICF) to estimate a value of N/O. In the higher-ionization objects a correction is needed for unobserved O^{+3}, as indicated by the amount of He^{++} compared to He^{+}, and the [N II] lines are exceedingly weak, making the N abundance uncertain. For C, there are no collisionally excited lines in the optical spectral region at all. Only recently have investigators attempted to use weak recombination lines (RELs) of N, O, and C to derive CNO abundances, with most investigations finding significantly higher CNO abundances from RELs than from collisionally excited lines (CELs) for O and N; this is the the well-known "abundance discrepancy factor" (see, e.g., Liu et al. 2006).

However, in the ultraviolet there are strong collisionally excited lines of the higher ionization states of N and several ionization states of C and O. Since the 1980s extensive observations of these lines in numerous PNs have been made

* Based on observations with the NASA/ESA *Hubble Space Telescope* obtained at the Space Telescope Science Institute, which is operated by the Association of Universities for Research in Astronomy, Incorporated, under NASA contract NAS5-26555.

with the *IUE* satellite see, e.g., the review by Koeppen & Aller 1987 and provided the first empirical data on C/H in the shells ejected from LIMS, as well as more accurate N/H values. However, *IUE* had limitations on the accuracy for which the emission line could be measured, due to the vidicon camera detector having a limited 8 bit encoding capability and significant fixed-pattern noise. Moreover, in order to assure photometric accuracy, the UV observations had to be made with a large $10'' \times 20''$ oval aperture that was essentially impossible to match to ground-based optical spectrometers. This mis-match of apertures affected all abundance calculations of PNs when UV- and optical-band spectra were analyzed in tandem.

Despite its limitations, numerous investigations of CNO abundances in PNs from *IUE* observations were published during the 1980s and beyond. Early on Dufour (1991) and Perinotto (1991) compiled many of the earlier *IUE* results for individual PNs to evaluate CN production and conversion in PNs of Peimbert Types I and II (Peimbert & Torres-Peimbert 1983). Kingsburgh & Barlow (1994) used *IUE* and optical data to measure abundances in a large sample of southern planetaries. Rola & Stasińska (1994) compiled published UV and optical line strengths of carbon to determine the fraction of PNs that are C-rich. Kwitter and Henry combined reprocessed (NEWSIPS) *IUE* spectra of 20 galactic PNs with their own optical data (supplemented by the literature) to determine abundances of C, N, and O (Henry et al. 1996; Kwitter & Henry 1996, 1998; Henry et al. 2000). With the launch of the *Hubble Space Telescope* (*HST*) in 1990, a new era of UV spectroscopy capabilities for nebular studies was born with the Faint Object Spectrograph (FOS), which featured linear detectors of high dynamic range for spectroscopy at both UV and optical wavelength regions through apertures of identical size. The replacement of FOS with the Space Telescope Imaging Spectrograph (STIS) in 1997 added a two-dimensional long-slit capability and combined UV–optical spectroscopy. This paper is the first to employ this new feature for a detailed study of CNO abundances in several Galactic PNs.

The goal of the project described in this paper is to measure accurate C, N, and O abundances in PNs using new *HST* STIS observations spanning a wavelength range of 1150–10270 Å. We observed 10 PNs representing a broad range in N abundance, but with overall metallicities close to solar. We present the details concerning the observations in Section 2. Section 3 contains the results regarding the abundances and nebular properties of each nebula, and we discuss the implications of these results in Section 4. Finally, our conclusions regarding our empirical results are presented in Section 5. In a subsequent paper (R. J. Dufour et al. 2015, in preparation) we will compute photoionization models of each of our objects in order to derive the central star properties. From these results we will derive the birth mass of each progenitor, combine it with our C and N abundances in the current paper, and evaluate several sets of published stellar model predictions of C and N abundances in PNs.

2. OBSERVATIONS

2.1. Target Selection

The *HST* Cycle 19 TAC awarded us 32 orbits to observe 10 PNs with STIS. We strove for three objectives in establishing our target list: (1) a narrow metallicity range (as measured by O/H) centered on the solar value; (2) a large range in N/O; and (3) the highest surface brightness (and good angular size when practical), all inferred from optical data employed in our earlier studies of Galactic PNs. We first identified a large set of potential STIS targets for their favorable observability (surface brightness, total flux through the slit, etc). For science reasons noted above, we then selected PNs with roughly solar O/H abundances $[8.55 < 12 + \log(\mathrm{O/H}) < 8.80]$. From these we selected semi-finalists with a wide range of N/O. Any very similar targets were culled using excitation, morphology, and electron temperature criteria in order to select 10 finalists requiring 32 STIS orbits.

The 10 finalists initially selected were IC 418, IC 2165, IC 4593, NGC 2440, NGC 3242, NGC 5882, NGC 6537, NGC 6572, NGC 6778, and PB6 (ESO-213-7). In developing the "Phase I" observation template, we identified permissible slit orientations, given the *HST* observation windows, and chose ones near or on the central stars that covered a good mix of ionization structure (evident from narrow band WFPC2 images in most cases) and high surface brightness rims, knots, etc. After submitting the observation template, we received a "red-flag" warning from the project scientist and STIS safety officer that we needed to provide evidence from *IUE* UV spectra that each CSPN was "safe" for observation by the UV MAMA detectors with the low-resolution UV gratings (G140L and G230L)—otherwise, we would have to move the slit centers $5''$ or more away from the stars to protect the detectors. To put it mildly, this was a surprise and required an entire re-evaluation of our object selection and slit locations, based on STIS safety "rules" versus optimum science input. After constructing *IUE* spectra of our 10 targets, we found that four had "unsafe" central stars for which the STIS slit had to be at least $5''$ away from the stars. These "unsafe" PNs were IC 4593, NGC 3242, IC 418, and NGC 6572. Given the large angular size of NGC 3242, we could place the slit $5''$ from the central star without sacrificing much in the way of surface brightness and ionization structure, but the other three PNs had to be replaced by larger PNs with "safe" central stars or large angular size and similar N/O ratios to the original objects. After studying the Kwitter & Henry PN abundance database (hereafter, the KH database, comprising published results from observations over the past two decades by Kwitter, Henry, and collaborators) and the *IUE* spectral archives, we chose IC 3568, NGC 5315, and NGC 7662 as replacements.

Figure 1 shows the final 10 PNs chosen with the slit positions and orientations that were possible given *HST* observation windows and STIS safety constraints. The targets, coordinates, and slit positions are given in Table 1. Most images were obtained with *HST*/WFPC2, in multiple pass-bands, and are presented in false-color. The images are all on the same spatial scale, with NE to the upper left; see the figure caption for details. While in some cases we were able to include the central star in the slit, in others we were obligated to offset the slit by $5''$.

Because of the length of time involved in obtaining approval for the UV observations on an individual object-by-object basis and the changes in some of the PN targets requiring the development of a new Phase II template, the first observations were not begun until 2012 January (NGC 3242) and completed a year later (2013 January; NGC 2440).

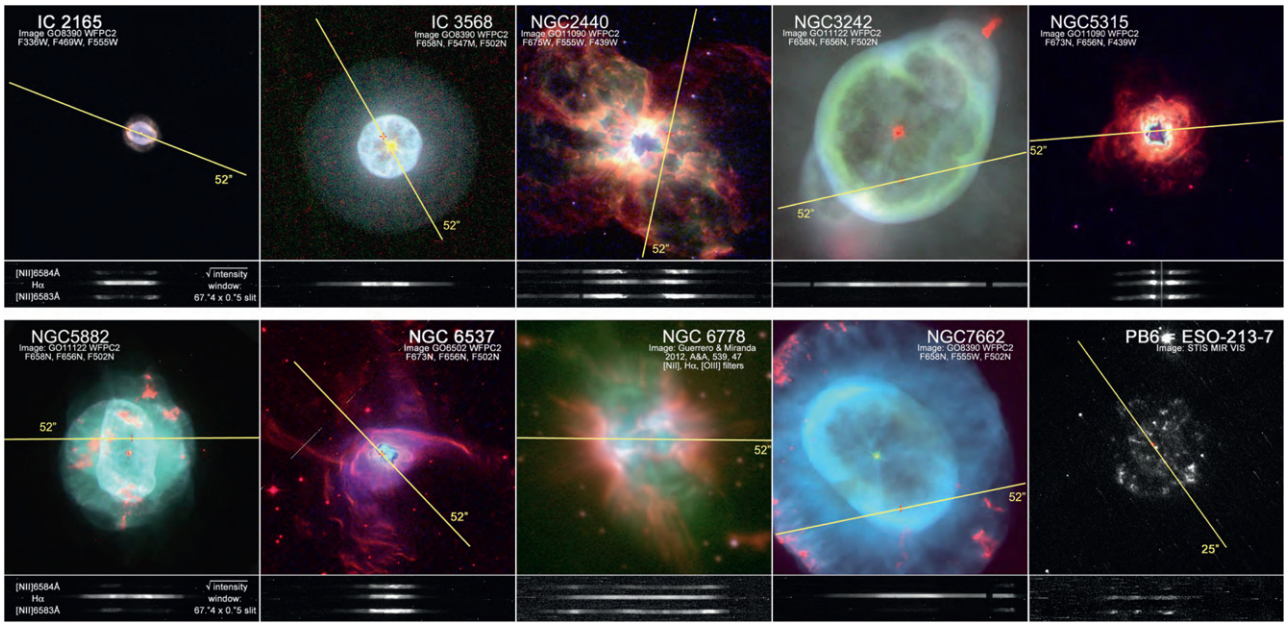

Figure 1. Slit positions and orientations (yellow lines) on multi-filter images of our target PNs. The image of PB6 is an exception: it is the pointing exposure for the STIS observations. Portions of the G750M STIS spectrum are shown below each image. They show the emission-line intensity distributions of the Hα and [N II] lines that are characteristic of emission lines in our STIS data. These "line profiles" are convolved in the dispersion direction by thermal broadening and internal motions within the nebulae. The actual slit location of NGC 2440 and NGC 7662 may have been offset by up to 2″ from the yellow line.

Table 1
Slit Reference Positions and Extraction Regions

Nebula	Slit Reference Position R.A. (J2000)	Slit Reference Position Decl. (J2000)	Offset from CS (arcsec)	Orient (deg)	Extract Bounds[a] (arcsec)
IC 2165	6 21 42.775	−12 59 12.96	0	68.650	−6.12: +4.68
IC 3568	12 33 07.340	+82 33 50.40	0.5 E	29.684	−2.52: −0.72, +0.10: +1.62
NGC 2440	07 41 54.875	−18 12 29.97	Unknown[b]	−13.350	−9.80: +1.26
NGC 3242	10 24 46.107	−18 38 37.14	4.5 S	−77.350	−7.20: +9.00
NGC 5315	13 53 56.980	−66 30 50.60	0.4 N	−85.345	−1.80: +0.36, +0.99: +3.60
NGC 5882	15 16 49.938	−45 38 57.19	0.0	−90.350	−2.70: +2.52
NGC 6537	18 05 13.129	−19 50 34.62	0.0	−136.350	−1.80: +2.16
NGC 6778	19 18 24.939	−01 35 47.41	0.0	89.651	−3.24: −0.36, +0.72: −3.60
NGC 7662	23 25 53.600	+42 32 00.50	5.5 S	101.649	−2.52: +5.40
PB6	10 13 15.989	−50 19 59.13	0.0	34.646	−6.48: −1.08, +0.00: +6.12

[a] Extraction window along the slit, relative to reference position; multiple extractions were summed.
[b] Target acquisition failed: position uncertain and optical position differs from UV.

2.2. Observing Strategy

Our observing strategy was designed to achieve our primary science goals. The first goal was to obtain spectra of each target that covered the full, uninterrupted spectrum from UV through optical (1150 Å through 10150 Å), with sufficient resolution and sensitivity to derive nebular gas diagnostics and ionic abundances of all critical species. We achieved these goals by allocating a full orbit to obtaining UV spectra with the G140L, G230L, and G230M gratings, and two (or for the faintest targets, three) orbits to obtain optical spectra with the G430L, G430M, G750L, and G750M gratings. We balanced the need for good spectral resolution with the need for high sensitivity by using the $52'' \times 0''.2$ slit for the low-resolution gratings and $52'' \times 0''.5$ for the medium-resolution gratings. The higher-resolution gratings allowed us to resolve blends of a few critical lines: C III] λ1906 from λ1909, H I λ4341 from [O III] λ4363, H I λ6563 from [N II] $\lambda\lambda$6548 and 6583, [S III] λ6312 from [O I] λ6300, and [S II] λ6716 from λ6731.

The second goal was to make *co-spatial* observations (i.e., with identical positioning and orientation of the apertures) of each target in all spectra, in order to avoid highly uncertain corrections for ionization stratification. The brightness limits (local and global) for the STIS/MAMA detectors, the required segregation of MAMA and CCD exposures to separate visits, and the need to provide some flexibility in the final slit orientation for scheduling reasons presented some challenges to the design of our observing program. All of our targets are spatially extended (a few are larger than the spatial extent of the slit for MAMA exposures), most nebulae have high UV surface brightness, and many of the central stars are very bright in the UV. On the other hand, the bright, central portion of these nebulae is precisely where we expected to detect changes

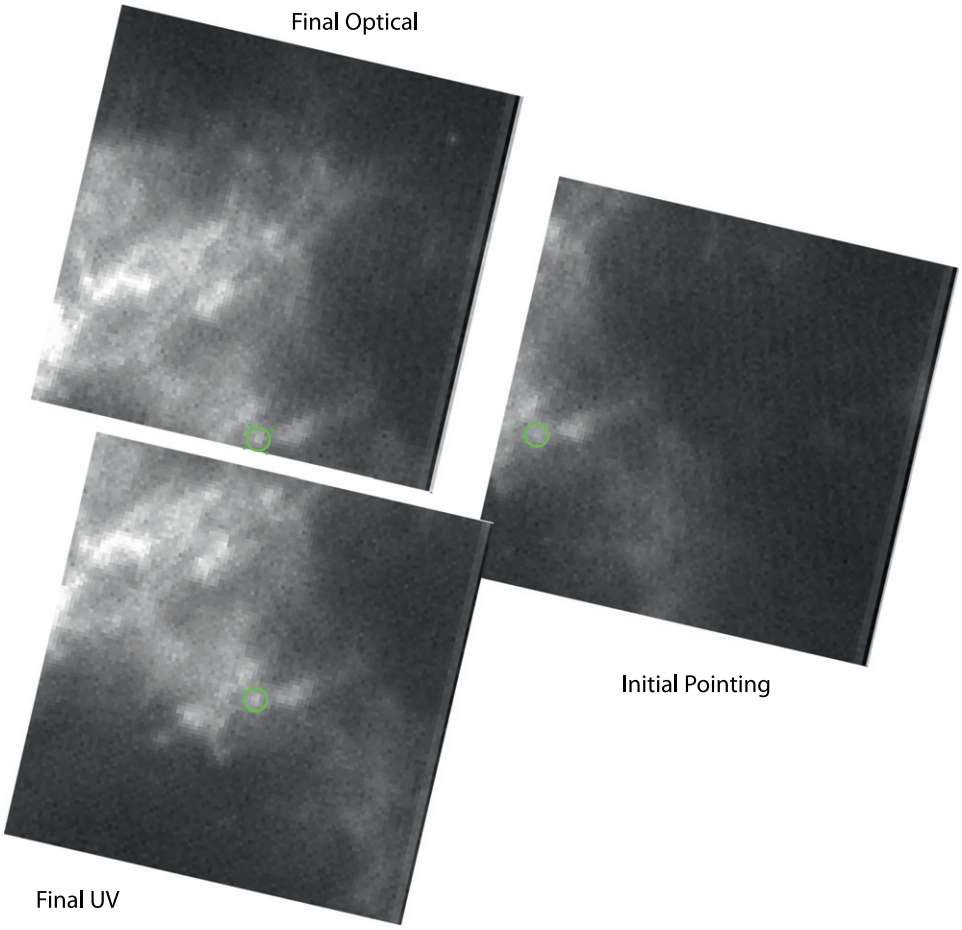

Figure 2. Acquisition images of NGC 2440 at the initial pointing, and the final positions for the UV and optical (northeast is in the upper left). A green marker is superimposed on each image, indicating a nebular knot in common; the location of the knot indicates that the final location of the slit reference position in the optical band lies almost directly south of the UV position by about 2″17.

in ionization with position (a third goal of our observing strategy). We therefore constrained our MAMA visits to occur close in time to the initial CCD visits, in order to use the same guide stars for the MAMA visit aquisition.

2.3. Data Acquisition

The observations were executed between 2012 January 15 and 2013 January 28, with the UV (MAMA) and optical (CCD) visits occurring within a few days of each other. See the observing log for this program in Table 2. Most observations were successful, except for a failure with the NUV exposures for NGC 6537 (which was subsequently repeated some weeks later) and an acquisition failure for NGC 2440. All of the exposures for NGC 2440 were executed, but our examination of the acquisition images shows that the UV and optical slit positions were not perfectly co-spatial. We analyzed, with the help of STScI staff, the failed acquisition sequence for NGC 2440. The acquisitions begin with a short exposure of a $5'' \times 5''$ field within STIS 50CCD aperture at the initial spacecraft pointing. The next step, locating the brightest feature in the field, failed for both the UV and CCD visits. The subsequent offset in each visit placed the final slit position for the UV and optical-band exposures in different locations. Figure 2 shows the acquisition images at the initial pointing and the final positions for the UV and optical (northeast is in the upper left). A green marker is superimposed on each image, indicating a nebular knot in common; the location of the knot indicates that the final location of the slit reference position in the optical band lies almost directly south of the UV position by about 2.″17. In a forthcoming paper we will analyze the emission-line profiles for the brighter nebulae in our sample. Our initial profile analysis for NGC 2440 suggests that the ionization stratification (and, perhaps, extinction) varies significantly with position, so that the ionic abundance analysis involving UV emission lines may not correspond well to that of the optical lines. While the emission-line fluxes are presented here (see Section 2.4), it must be kept in mind that the UV and optical data are from different regions in the nebulae that may have somewhat different ionization.

2.4. Data Reduction and Spectral Extractions

The data were reduced and calibrated using the CALSTIS v2.36 pipeline (ca. 2011 May 27). The processing depends on the detector in use (MAMA or CCD) and is described in detail by Bostroem & Proffitt (2011). Briefly, the processing includes overscan and bias correction (CCD only) or re-binning by a factor of 2 (MAMA only), bad pixel flagging, dark and flat-field corrections, fringe correction (CCD G750 only), calibrations of the world coordinate system (wavelength and spatial extent of the slit), flux calibration (see Holland et al. 2014, and references therein), and geometric rectification.

Table 2
Observing Log for GO 126000

Nebula	UT Date	Data Set	Grating/ Cent. Wave	Dispersion (Å pixels^{-1})	Slit Width[a] (arcsec)	T_{Exp} (s)
IC 2165	2012 Apr 28	OBRZ14010	G140L/1425	0.60	0.2	2280
	⋯	OBRZ14020	G230L/2376	1.58	0.2	1946
	⋯	OBRZ14030	G230M/1884	0.09	0.5	346
	2012 Apr 30	OBRZ13010	G430L/4300	2.75	0.2	360
	⋯	OBRZ13020	G430M/4451	0.28	0.5	210
	⋯	OBRZ13040	G750L/7751	4.92	0.2	360
	⋯	OBRZ13030	G750M/6581	0.56	0.5	165
IC 3568	2012 Jul 15	OBRZ02010	G140L/1425	0.60	0.2	2624
	⋯	OBRZ02020	G230L/2376	1.58	0.2	2146
	⋯	OBRZ02030	G230M/1884	0.09	0.5	546
	2012 Jul 13	OBRZ01010	G430L/4300	2.75	0.2	456
	⋯	OBRZ01020	G430M/4451	0.28	0.5	276
	⋯	OBRZ01040	G750L/7751	4.92	0.2	426
	⋯	OBRZ01030	G750M/6581	0.56	0.5	276
NGC 2440	2013 Jan 28	OBRZ27010	G140L/1425	0.60	0.2	2272
	⋯	OBRZ27020	G230L/2376	1.58	0.2	2862
	⋯	OBRZ27030	G230L/2376	1.58	0.2	882
	⋯	OBRZ27040	G230M/1884	0.09	0.5	504
	⋯	OBRZ27050	G230M/2338	0.09	0.5	564
	2013 Jan 21	OBRZ26010	G430L/4300	2.75	0.2	351
	⋯	OBRZ26020	G430M/4451	0.28	0.5	171
	⋯	OBRZ26040	G750L/7751	4.92	0.2	351
	⋯	OBRZ26030	G750M/6581	0.56	0.5	81
NGC 3242	2012 Jan 21	OBRZ05010	G140L/1425	0.60	0.2	2242
	⋯	OBRZ05020	G230L/2376	1.58	0.2	1968
	⋯	OBRZ05030	G230M/1884	0.09	0.5	328
	2012 Jan 15	OBRZ04010	G430L/4300	2.75	0.2	360
	⋯	OBRZ04020	G430M/4451	0.28	0.5	189
	⋯	OBRZ04040	G750L/7751	4.92	0.2	330
	⋯	OBRZ04030	G750M/6581	0.56	0.5	180
NGC 5315	2012 Feb 27	OBRZ17010	G140L/1425	0.60	0.2	2660
	⋯	OBRZ17020	G230L/2376	1.58	0.2	2122
	⋯	OBRZ17030	G230M/1884	0.09	0.5	522
	2012 Feb 26	OBRZ16010	G430L/4300	2.75	0.2	405
	⋯	OBRZ16020	G430M/4451	0.28	0.5	315
	⋯	OBRZ16040	G750L/7751	4.92	0.2	465
	⋯	OBRZ16030	G750M/6581	0.56	0.5	285
NGC 5882	2012 Apr21	OBRZ11010	G140L/1425	0.60	0.2	2328
	⋯	OBRZ11020	G230L/2376	1.58	0.2	2118
	⋯	OBRZ11030	G230M/1884	0.09	0.5	318
	2012 Apr 19	OBRZ10010	G430L/4300	2.75	0.2	360
	⋯	OBRZ10020	G430M/4451	0.28	0.5	210
	⋯	OBRZ10040	G750L/7751	4.92	0.2	360
	⋯	OBRZ10030	G750M/6581	0.56	0.5	213
NGC 6537	2012 Mar 01	OBRZ31010	G140L/1425	0.60	0.2	2304
	2012 Apr 20	OBRZ32010	G230L/2376	1.58	0.2	1522
	⋯	OBRZ32020	G230M/1884	0.09	0.5	222
	2012 Feb 29	OBRZ30010	G430L/4300	2.75	0.2	363
	⋯	OBRZ30020	G430M/4451	0.28	0.5	213
	⋯	OBRZ30040	G750L/7751	4.92	0.2	363
	⋯	OBRZ30030	G750M/6581	0.56	0.5	183
NGC 6778	2012 Aug 02	OBRZ20010	G140L/1425	0.60	0.2	2274
	⋯	OBRZ20020	G230L/2376	1.58	0.2	1960
	⋯	OBRZ20030	G230M/1884	0.09	0.5	320
	2012 Jul 31	OBRZ19010	G430L/4300	2.75	0.2	363
	⋯	OBRZ19020	G430M/4451	0.28	0.5	183
	⋯	OBRZ19040	G750L/7751	4.92	0.2	363
	⋯	OBRZ19030	G750M/6581	0.56	0.5	183
NGC 7662	2012 Oct 09	OBRZ08010	G140L/1425	0.60	0.2	2296
	⋯	OBRZ08020	G230L/2376	1.58	0.2	1994
	⋯	OBRZ08030	G230M/1884	0.09	0.5	394
	2012 Oct 04	OBRZ07010	G430L/4300	2.75	0.2	381
	⋯	OBRZ07020	G430M/4451	0.28	0.5	204

Table 2
(Continued)

Nebula	UT Date	Data Set	Grating/ Cent. Wave	Dispersion (Å pixels^{-1})	Slit Width[a] (arcsec)	T_{Exp} (s)
	⋯	OBRZ07040	G750L/7751	4.92	0.2	324
	⋯	OBRZ07030	G750M/6581	0.56	0.5	204
PB6	2012 Apr 25	OBRZ23010	G140L/1425	0.60	0.2	2428
	⋯	OBRZ23020	G230L/2376	1.58	0.2	3058
	⋯	OBRZ23030	G230L/2376	1.58	0.2	2154
	⋯	OBRZ23040	G230M/1884	0.09	0.5	454
	2012 Apr 26	OBRZ22010	MIRVIS	⋯	⋯	22
	⋯	OBRZ22020	G430L/4300	2.75	0.5	303
	⋯	OBRZ22030	G430M/4451	0.28	0.5	123
	⋯	OBRZ22050	G750L/7751	4.92	0.2	303
	⋯	OBRZ22040	G750M/6581	0.56	0.5	63

[a] Slit width of 0.″2 corresponds to 3.94 pixels for the CCD and 8.13 pixels for the MAMA detectors; slit width of 0.″5 corresponds to 9.85 pixels for the CCD and 20.33 pixels for the MAMA. As described in the *STIS Instrument Handbook* (Biretta et al. 2015), for extended sources the spectral resolution is limited by the slit width for all settings.

The pipeline is capable of producing a variety of calibrated data products, but our spatially extended targets require custom spectral extraction from the calibrated, two-dimensional spectrograms: the *_sx2.fits files (hereafter, SX2). These products include a science array, a bit-encoded mask array that records detector or processing anomalies at the pixel level, and a variance array.

For each PN we examined the SX2 files and the emission profiles of the brighter lines from all gratings to determine the optimal spatial region for extraction. Since the spatial scales differ between the MAMA and CCD detectors (and between some CCD gratings), we developed a utility to extract regions that are spatially matched, rounded to the nearest whole pixel, for all gratings for a given target. The extraction regions are given in the last column of Table 1, in arcseconds relative to the slit reference position. Note that the spatial extent of the extraction regions is rather large, spanning nearly the entire extent of the target, so rounding the extremes to integral pixels has no significant effect on the relative fluxes between gratings. The extractions to one dimension were derived from the SX2 images by averaging pixel values at each wavelength (column) over the specified spatial range, normalizing by the extraction area in pixels, and converting from surface brightness to flux density. All pixels marked as *bad* in the pixel mask were excluded except for those flagged as affected by flat-field blemishes, noisy background, and excessive dark rate, as long as no other flags applied. While ignoring these flags adds some additional uncertainty to the average value, the final average is usually dominated by well-exposed pixels where these pathologies are unimportant. In rare instances (at the edge of the MAMA detectors) all pixels were flagged as bad, so the average flux at such wavelengths was set to zero. No background subtraction was performed at this stage. In cases where the slit was positioned close to or included the central star, special care was taken to minimize stellar contamination of the nebular spectrum. In the end, signal-to-noise ratio (S/N) considerations and scattering of the starlight by dust in some nebulae compelled us to accept some stellar light in the cases of IC 3568, NGC 5315, and NGC 5882.

2.5. Measurements

Emission-line fluxes were measured using the IRAF[8] splot package. Most lines were observed only in the *L* gratings. Regions with important closely spaced lines were also observed with the medium-resolution *M* gratings, through a wider slit; see Table 2. Measurements of the better-resolved *M* spectra yielded ratios for these lines, which were then used to apportion the summed flux measured on the *L* spectra. For weak lines detected only in the *M* spectra, the measured flux was multiplied by 2.5, the ratio of the *L* and *M* slit widths. Figures 3 and 4 show UV and optical spactrograms, respectively, for IC 2165 as examples of the data quality and spectral range. Numerous emission lines are identified; inset graphs show enlargements of some line complexes.

Line intensities are given in Tables 3 and 4, normalized to $F(H\beta) = 100$. The columns are, in order: the wavelength of the emission line; the line identification by ion; $f(\lambda)$, the value of the reddening function at that wavelength; $F(\lambda)$, the observed line flux; and $I(\lambda)$, the corrected line intensity with its uncertainty. Stellar and stellar+nebular composite lines are noted, as are lines that may be affected by artifacts in the 2D spectrogram. At the end of the table are, for each nebula, the calculated value of *c*, the logarithmic reddening parameter; the expected, zero-reddening ratio of $F(H\alpha)/F(H\beta)$ for the derived nebular temperature (from T[O III]) and density (usually from N[S II]); and the observed $F(H\beta)$ through the extraction window. Note that we give the line intensities for NGC 2440 in two columns: one for the UV (MAMA) spectra and another for the optical (CCD) spectra. Although the regions are in principle distinct, we normalize the fluxes to $F(H\beta)$ as measured in the optical and determine the diagnostics and abundances as if they were from the same location (see Section 3.2.3); we call out the potential for problems in the results below.

Uncertainties were estimated in the following way. For each line, we obtained the rms continuum value on either side (the *m* key in splot); sometimes only one side was amenable for measurement. We took the average rms of the two sides and multiplied it by the line FWHM (*k* key or via deblending

[8] IRAF is distributed by the National Optical Astronomy Observatory, which is operated by the Association of Universities for Research in Astronomy (AURA) under cooperative agreement with the National Science Foundation.

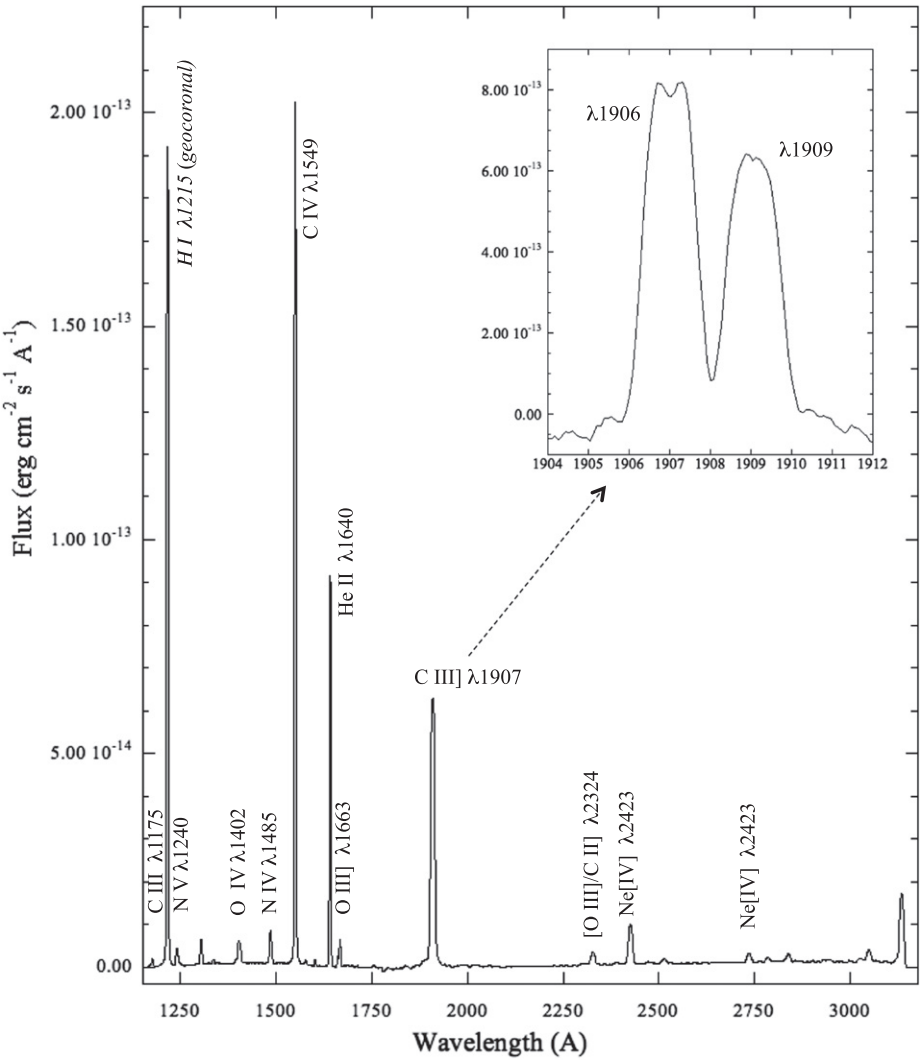

Figure 3. Spectrum of IC 2165 over the UV wavelength range. Numerous emission lines are identified. The inset shows an enlarged view of the closely spaced lines of C III] λλ1906, 1909.

option in *splot*) to obtain the line flux uncertainty. The emission-line fluxes along with their uncertainties constitute the input for our abundance determinations using ELSA, our five-level atom code (Johnson et al. 2006). ELSA propagates the uncertainties though the calculations, including the intensities, diagnostics, and abundances. The first step in the analysis is to generate a table of line intensities that have been corrected for interstellar reddening and for contamination of the hydrogen Balmer lines by coincident recombination lines of He^{++}. In addition, ELSA can disentangle some unresolved line blends (here, [Ne III] λ3968 and Hϵ λ3970) when one or both of the lines have a known ratio to another measured line. We corrected for the effects of reddening using the function of Savage & Mathis (1979) in the optical region and Seaton (1979) in the ultraviolet. Details of the analysis using ELSA are described in Milingo et al. (2010).

A few very weak emission lines were noted in three objects that we were unable to identify. These are noted in Table 5 by wavelength and the nebula in which they were found; the intensities were comparable to the noise in the surrounding continuum. Though weak, the lines appear in the SX2 images to have profiles similar to other, well-exposed nebular lines rather than artifacts (e.g., hot pixels or charge trails). We note them here in the hope that future investigations may be able to make use of them.

3. RESULTS

3.1. Plasma Diagnostics and Abundances

We present the plasma diagnostics in Table 6. The [O III] temperature is derived from the I(λ4343)/I(λ5007) ratio. Where available, the [N II] temperature is derived from the I(λ5755)/I(λ6584) ratio; otherwise, based on previous work (Kwitter & Henry 2001): if He II λ4686 is detected, as it is in all PNs here, we adopt the carefully derived result from Kaler (1986) that applies under this condition, i.e., T[N II] = 10,300 K. If the required lines have been detected, we also report values of T[O II] from I(λ7323)/I(λ3727), but owing to the high uncertainty associated with these derived temperatures they are not used in any calculations. The T[S II] diagnostic from I(λ[4068 + 4076])/I(λ[6717 + 6731]) failed to give reliable results because the emission is quite weak, and the λ4068 + 4076 doublet is potentially blended with weak recombination lines. If the [S III] lines λ6312 and one of λ9069 or λ9532 are available, T[S III] is calculated and, if it is within 5000 K of T[O III], we use it to derive the abundances of S^{+2}

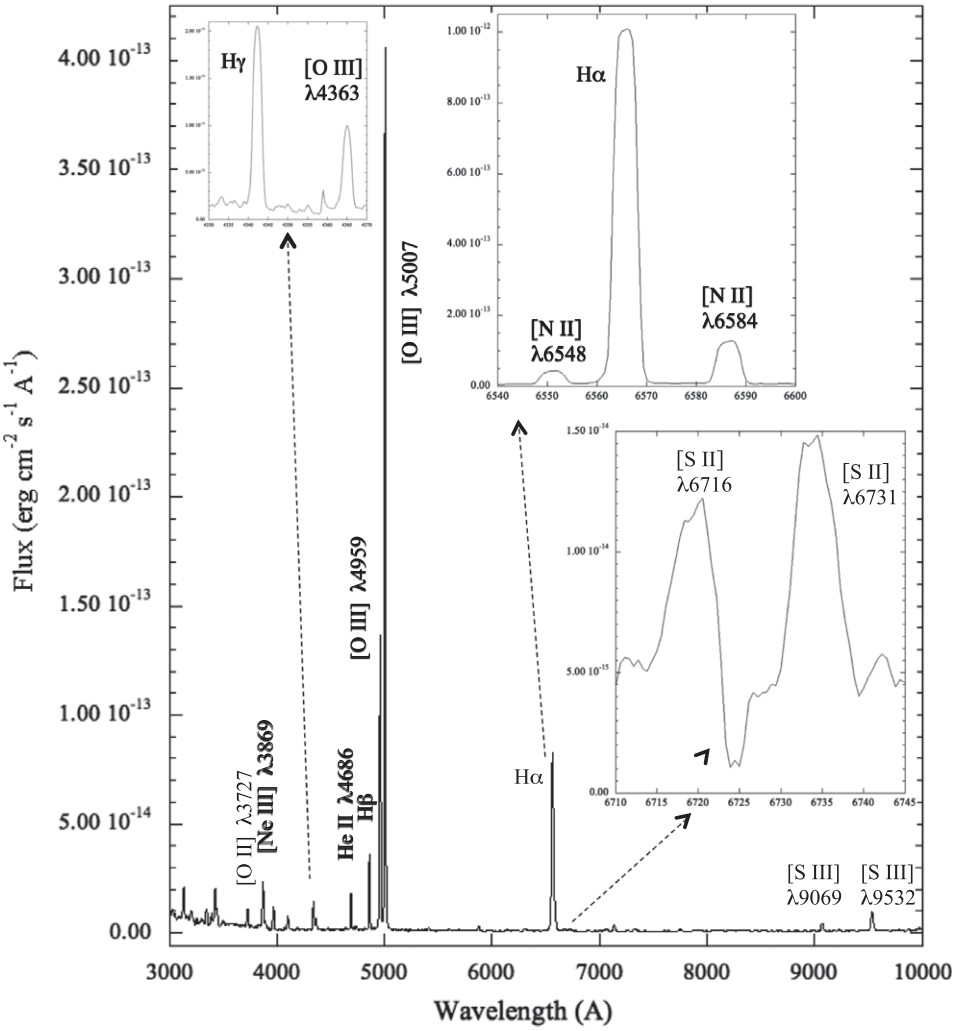

Figure 4. Spectrum of IC 2165 over the optical wavelength range. Numerous emission lines are identified. The insets show enlarged views of three line complexes: [S II] λλ6716, 6731; [N II] λλ6548, 6584 straddling Hα; and the region from Hγ to [O III] λ4363.

and Cl^{+2}. In general, T[O III] is used for both helium ions and other ions in states +2 or above; T[N II] is used for the other singly ionized species. Electron densities are calculated using ratios of [S II] I(λ6717)/I(λ6731) and C III] I(λ1909)/I(λ1906). If only one density diagnostic is available, it is used for all calculations. If both are available, N[S II] is used to calculate abundances of singly ionized species, and N[C III] is used for the higher-ionization species.

Ionic abundances derived using ELSA are given in Table 7. The first column lists the ion and wavelength used to calculate the values in each row; the adopted value for the ionic abundance corresponds to the mean of all the observed lines of that ion, weighted by raw observed flux, and is used in subsequent calculations. Measured lines contaminated by stellar emission (indicated in Tables 3 and 4) are excluded from further analysis. Values of the ICF that was derived to compute total abundances are shown at the end of each ion listing; these have been calculated in ELSA as described in Kwitter & Henry (2001), except for carbon, which was not studied in that paper. Here we use the following:

$$\mathrm{C/H} = \frac{\mathrm{C^{++}}}{\mathrm{H^{+}}} \times \mathrm{ICF(C)},$$

where

$$\mathrm{ICF(C)} = \frac{\left(\mathrm{O^{+}} + \mathrm{O^{++}}\right)}{\mathrm{O^{++}}} \times \frac{\left(\mathrm{He^{+}} + \mathrm{He^{++}}\right)}{\mathrm{He^{+}}}.$$

The total elemental abundances are shown in Table 8. For C- and N-related parameters, we show both the values derived using ICFs and those obtained by summing abundances of observed ions. Note that abundances of O, Ne, S, and Ar presented here are ICF values. The last two columns give values for the Sun (Asplund et al. 2009) and Orion (Esteban et al. 2004).

3.2. Individual Nebulae

Here we discuss the abundance results for eight of the 10 PNs we observed. NGC 6537 and NGC 6778 are not included since the low S/N of the STIS data prevented any meaningful homogeneous abundance analysis. The emission-line intensities for these excluded objects, presented in Table 4, should inform future investigators of the stronger UV emission lines and of the approximate scaling from the UV to optical band.

Table 3
Fluxes and Intensities I

Wave			IC 2165		IC 3568		NGC 2440 UV		NGC 2440 Opt		NGC 3242		NGC 5315	
(Å)	ID[c]	f(λ)	F(λ)	I(λ)	F(λ)	I(λ)	F(λ)	I(λ)	F(λ)	I(λ)	F(λ)	I(λ)	F(λ)	I(λ)
1175	C III	1.849	2.03	16.0 ± 1.1	3.18[a]	7.05 ± 1.11[a]	1.30	10.1 ± 0.6	⋯	⋯	27.4	30.7 ± 0.8	⋯	⋯
1241	N V	1.636	7.07	44.1 ± 2.4	22.2[a]	45.0 ± 2.8[a]	20.9	128. ± 2.	⋯	⋯	1.84	2.03 ± 0.17	0.937[a]	6.94 ± 5.07[a]
1247	C III	1.620	⋯	⋯	⋯	⋯	⋯	⋯	⋯	⋯	5.81	6.41 ± 0.17	0.641[a]	5.21 ± 3.76[a]
1266	Fe II	1.569	⋯	⋯	⋯	⋯	⋯	⋯	⋯	⋯	2.55	2.81 ± 0.15	⋯	⋯
1305	O I	1.478	⋯	⋯	⋯	⋯	⋯	⋯	⋯	⋯	4.38	4.79 ± 0.18	0.353	2.39 ± 0.22
1324	[Mg V]?	1.438	⋯	⋯	⋯	⋯	0.795	3.91 ± 0.58	⋯	⋯	⋯	⋯	⋯	⋯
1336	C II	1.415	1.09	5.29 ± 0.34	⋯	⋯	1.26	6.02 ± 0.56	⋯	⋯	5.91	6.45 ± 0.15	⋯	⋯
1344	O IV + N II	1.400	⋯	⋯	⋯	⋯	0.774	3.65 ± 0.60	⋯	⋯	2.52	2.74 ± 0.11	2.60[a]	15.9 ± 0.8[a]
1370	O V	1.354	⋯	⋯	0.947[a]	1.70 ± 0.32[a]	0.774	3.48 ± 0.49	⋯	⋯	⋯	⋯	⋯	⋯
1394	Si IV	1.316	⋯	⋯	⋯	⋯	⋯	⋯	⋯	⋯	0.588	0.637 ± 0.109	⋯	⋯
1402	S IV] +O IV]?	1.307	10.9	47.2 ± 2.1	⋯	⋯	18.4	78.2 ± 1.4	⋯	⋯	8.05	8.72 ± 0.32	⋯	⋯
1417	S IV]?	1.292	0.224	0.950 ± 0.171	⋯	⋯	⋯	⋯	⋯	⋯	⋯	⋯	⋯	⋯
1423	S IV]?	1.286	0.087	0.368 ± 0.103	⋯	⋯	⋯	⋯	⋯	⋯	⋯	⋯	⋯	⋯
1485	N IV]	1.231	12.1	47.9 ± 2.0	<0.94	⋯	76.6	300. ± 4.	⋯	⋯	9.41	10.2 ± 0.2	<0.43	<2.1
1549	C IV	1.184	254.	957. ± 39.	23.5[b]	39.1 ± 2.44[b]	146.	541. ± 8.	⋯	⋯	39.0	41.9 ± 0.7	35.4[b]	164. ± 91.[b]
1575	[Ne V]	1.168	0.949	3.51 ± 0.51	⋯	⋯	20.0	73.1 ± 1.2	⋯	⋯	6.65	7.14 ± 0.18	⋯	⋯
1602	[Ne IV]	1.153	1.69	6.13 ± 0.50	⋯	⋯	3.03	10.9 ± 0.4	⋯	⋯	1.33	1.43 ± 0.20	⋯	⋯
1640	He II	1.136	98.2	350. ± 14.	12.8	20.9 ± 1.8	146.	516. ± 7.	⋯	⋯	290.	311. ± 5.	8.91	38.7 ± 20.7[b]
1660	O III]	1.129	2.47	8.75 ± 0.46	1.92	3.12 ± 0.58	4.13	14.5 ± 0.6	⋯	⋯	4.59	4.92 ± 0.20	⋯	⋯
1666	O III]	1.128	7.14	25.2 ± 1.0	3.79	6.15 ± 0.62	10.3	36.0 ± 0.7	⋯	⋯	12.3	13.2 ± 0.3	⋯	⋯
1750	N III]	1.119	<2.8	<10.	<4.16	<4.16	54.7	189. ± 4.	⋯	⋯	8.35	8.94 ± 1.02	1.48	6.29 ± 1.35
1906	C III]	1.224	108.	424. ± 22.	41.7	70.6 ± 7.0	142.	552. ± 14.	⋯	⋯	126.	136. ± 3.	4.79	23.3 ± 2.8
1909	C III]	1.229	84.3	334. ± 19.	30.2	51.2 ± 7.2	107.	418. ± 14.	⋯	⋯	91.9	99.0 ± 2.6	7.16	35.0 ± 2.8
1981	[Fe VI]	1.357	⋯	⋯	⋯	⋯	⋯	⋯	⋯	⋯	3.25	3.54 ± 0.28	⋯	⋯
2135	He II	1.658	⋯	⋯	⋯	⋯	⋯	⋯	⋯	⋯	⋯	⋯	0.212	1.81 ± 0.76
2142	N II]?	1.662	⋯	⋯	⋯	⋯	2.13	13.4 ± 2.8	⋯	⋯	⋯	⋯	⋯	⋯
2187	He II + O III fl	1.653	⋯	⋯	⋯	⋯	⋯	⋯	⋯	⋯	1.07	1.19 ± 0.16	⋯	⋯
2214	He II	1.620	⋯	⋯	⋯	⋯	⋯	⋯	⋯	⋯	1.01	1.12 ± 0.15	⋯	⋯
2253	He II Pa 10–3	1.542	⋯	⋯	⋯	⋯	⋯	⋯	⋯	⋯	2.00	2.20 ± 0.19	⋯	⋯
2297	C III	1.431	0.777	3.86 ± 3.58	⋯	⋯	⋯	⋯	⋯	⋯	⋯	⋯	4.52[a]	28.7 ± 1.1[a]
2324	[O III]/C II]	1.359	9.80	44.9 ± 2.9	4.89	8.78 ± 1.68	19.2	86.4 ± 1.8	⋯	⋯	7.40	8.04 ± 0.20	2.28	13.2 ± 0.5
2385	He II Pa ϵ	1.204	1.33	5.11 ± 0.62	⋯	⋯	2.73	10.4 ± 1.5	⋯	⋯	3.82	4.11 ± 0.14	⋯	⋯
2423	[Ne IV]	1.118	28.3	98.8 ± 3.9	⋯	⋯	51.5	178. ± 3.	⋯	⋯	28.4	30.5 ± 0.5	⋯	⋯
2470	[O II]	1.025	0.76	2.38 ± 0.51	⋯	⋯	3.35	10.4 ± 1.0	⋯	⋯	0.535	0.570 ± 0.065	2.47	9.31 ± 0.32
2511	He II Pa δ	0.955	3.32	9.67 ± 0.67	⋯	⋯	4.37	12.6 ± 1.1	⋯	⋯	6.22	6.59 ± 0.12	⋯	⋯
2733	He II Pa γ	0.701	6.48	14.2 ± 0.7	⋯	⋯	8.71	18.9 ± 0.6	⋯	⋯	11.8	12.3 ± 0.4	⋯	⋯
2785	Fe II	0.658	3.56	7.43 ± 0.67	⋯	⋯	6.32	13.1 ± 0.5	⋯	⋯	⋯	⋯	⋯	⋯
2801	Fe II	0.645	⋯	⋯	⋯	⋯	0.428	0.875 ± 0.307	⋯	⋯	⋯	⋯	⋯	⋯
2837	O III fl	0.619	5.65	11.3 ± 0.6	5.49	7.16 ± 1.21	5.85	11.6 ± 0.5	⋯	⋯	10.9	11.4 ± 0.2	1.40	3.12 ± 0.25
2856	Fe II	0.606	⋯	⋯	⋯	⋯	2.28	4.46 ± 0.48	⋯	⋯	⋯	⋯	⋯	⋯
2872	Fe II	0.595	⋯	⋯	⋯	⋯	1.10	2.12 ± 0.41	⋯	⋯	⋯	⋯	⋯	⋯
2945	He I	0.550	⋯	⋯	2.31	2.92 ± 0.67	⋯	⋯	⋯	⋯	1.49	1.54 ± 0.24	0.71	1.45 ± 0.16
3025	O III fl	0.506	3.60	6.35 ± 0.79	1.84	2.29 ± 0.67	3.17	5.56 ± 0.83	⋯	⋯	6.86	7.08 ± 0.28	⋯	⋯
3048	O III fl	0.494	10.0	17.4 ± 0.9	3.09	3.82 ± 0.73	8.15	14.1 ± 1.2	⋯	⋯	18.4	18.9 ± 0.3	⋯	⋯
3133	O III fl	0.454	50.2	83.4 ± 1.9	⋯	⋯	48.9	80.9 ± 1.1	⋯	⋯	95.7	98.3 ± 1.5	6.21	11.2 ± 1.9
3203	He II Pa β	0.424	21.2	34.1 ± 9.9	⋯	⋯	⋯	⋯	18.3	29.4 ± 10.4	18.6	19.1 ± 1.6	8.17	14.1 ± 2.7
3340	O III fl	0.373	⋯	⋯	⋯	⋯	⋯	⋯	⋯	⋯	11.9	12.2 ± 1.4	⋯	⋯
3346	[Ne V]	0.371	30.6	46.4 ± 2.6	⋯	⋯	⋯	⋯	85.3	129. ± 3.	⋯	⋯	⋯	⋯
3426	[Ne V]	0.344	59.1	86.8 ± 2.6	⋯	⋯	⋯	⋯	174.	255. ± 5.	⋯	⋯	⋯	⋯
3448	He I/O III fl	0.337	24.7	36.0 ± 2.2	⋯	⋯	⋯	⋯	⋯	⋯	28.9	29.5 ± 2.2	⋯	⋯

Table 3
(Continued)

Wave			IC 2165		IC 3568		NGC 2440 UV		NGC 2440 Opt		NGC 3242		NGC 5315	
(Å)	ID[c]	f(λ)	F(λ)	I(λ)	F(λ)	I(λ)	F(λ)	I(λ)	F(λ)	I(λ)	F(λ)	I(λ)	F(λ)	I(λ)
3727	[O II]	0.292	29.7	41.2 ± 2.5	15.3	17.4 ± 2.5	⋯	⋯	80.4	111. ± 3.	11.2	11.3 ± 2.9	19.3	28.1 ± 0.4
3757	O III fl	0.284	⋯	⋯	⋯	⋯	⋯	⋯	⋯	⋯	8.22	8.36 ± 2.30	⋯	⋯
3770	He II + H11	0.280	⋯	⋯	3.05[d]	3.44 ± 1.39[d]	⋯	⋯	⋯	⋯	⋯	⋯	2.63	3.77 ± 0.27
3797	He II + H10	0.272	⋯	⋯	⋯	⋯	⋯	⋯	⋯	⋯	3.57	3.63 ± 1.49	3.23	4.59 ± 0.27
3820	He I	0.266	⋯	⋯	⋯	⋯	⋯	⋯	⋯	⋯	⋯	⋯	1.12	1.58 ± 0.26
3835	He II + H9	0.262	⋯	⋯	⋯	⋯	⋯	⋯	⋯	⋯	6.23	6.33 ± 0.61	5.21	7.31 ± 0.27
3869	[Ne III]	0.252	68.5	90.9 ± 2.4	69.8	77.8 ± 1.9	⋯	⋯	74.0	97.8 ± 2.5	93.5	95.0 ± 0.7	55.4	76.7 ± 0.5
3889	He I+ H8	0.247	12.2	16.1 ± 1.8	18.7	20.8 ± 1.2	⋯	⋯	8.59	11.3 ± 3.0	16.6	16.9 ± 0.4	12.2	16.9 ± 0.5
3968	[Ne III]	0.224	21.0[e]	27.1 ± 2.0[e]	22.2[e]	24.5 ± 0.8[e]	⋯	⋯	22.7[e]	29.1 ± 1.4[e]	29.5[e]	29.9 ± 0.5[e]	17.6[e]	23.5 ± 0.2[e]
3970	Hε	0.224	12.9[e]	16.6[e]	14.5[e]	16.0[e]	⋯	⋯	13.1[e]	16.8[e]	16.2[e]	16.4[e]	11.9[e]	15.9[e]
4026	He I + He II	0.209	3.79[d]	4.79 ± 1.68[d]	3.49	3.82 ± 0.48	⋯	⋯	⋯	⋯	⋯	⋯	2.08	2.73 ± 0.15
4071	[S II]	0.196	5.32[d]	6.63 ± 1.73[d]	⋯	⋯	⋯	⋯	6.73	8.36 ± 3.39	1.12	1.13 ± 0.52	6.33	8.16 ± 0.27
4100	He II	0.188	0.604[e]	0.745[e]	4.57(−2)[e]	4.95(−2)[e]	⋯	⋯	0.951[e]	1.17[e]	0.663[e]	0.671[e]	⋯	⋯
4101	Hδ	0.188	21.6[e]	26.6 ± 1.31[e]	25.7[e]	27.8 ± 0.7[e]	⋯	⋯	27.3[e]	33.6 ± 2.0[e]	26.9[e]	27.2 ± 0.6[e]	20.5	26.1 ± 0.2
4144	He I	0.177	⋯		⋯	⋯	⋯	⋯	⋯	⋯	⋯	⋯	0.350	0.439 ± 0.198
4195	N II/III?	0.163	4.85[d]	5.82 ± 1.11[d]	⋯	⋯	⋯	⋯	⋯	⋯	⋯	⋯	⋯	⋯
4267	C II	0.144	⋯	⋯	⋯	⋯	⋯	⋯	⋯	⋯	⋯	⋯	0.425	0.512 ± 0.137
4339	He II	0.124	1.15[e]	1.32[e]	8.31(−2)[e]	8.77(−2)[e]	⋯	⋯	1.80[e]	2.07[e]	1.18[e]	1.19[e]	⋯	⋯
4340	Hγ	0.124	39.8[e]	45.8 ± 0.8[e]	44.5[e]	46.9 ± 0.8[e]	⋯	⋯	42.5[e]	48.7 ± 1.2[e]	45.8[e]	46.1 ± 0.3[e]	39.6	46.5 ± 0.2
4363	[O III]	0.118	17.1	19.5 ± 0.6	8.78	9.23 ± 0.48	⋯	⋯	23.6	26.9 ± 1.2	13.0	13.1 ± 0.2	3.83	4.47 ± 0.20
4472	He I	0.090	3.30	3.65 ± 0.60	6.03	6.27 ± 1.20	⋯	⋯	3.52	3.89 ± 1.68	3.38	3.40 ± 0.33	5.75	6.46 ± 0.11
4542	He II	0.072	⋯	⋯	⋯	⋯	⋯	⋯	⋯	⋯	2.60	2.61 ± 0.59	⋯	⋯
4640	N III + O II	0.048	3.42	3.60 ± 0.86	2.91[d]	2.97 ± 1.02[d]	⋯	⋯	8.82	9.30 ± 2.75	3.84	3.85 ± 0.14	⋯	⋯
4650	C III + O II	0.045	⋯	⋯	⋯	⋯	⋯	⋯	⋯	⋯	⋯	⋯	23.1[b]	24.5 ± 0.4[b]
4686	He II	0.036	51.8	54.0 ± 1.1	3.65	3.71 ± 0.57	⋯	⋯	80.4	83.7 ± 0.5	49.5	49.6 ± 0.2	6.95[a]	7.28 ± 1.09[a]
4711	He I+ [Ar IV]	0.030	6.24	6.46 ± 0.89	1.41	1.43 ± 0.64	⋯	⋯	12.0	12.4 ± 0.6	5.97	5.98 ± 0.16	1.54	1.61 ± 0.13
4740	[Ar IV]	0.023	7.80	8.00 ± 0.89	2.67	2.70 ± 0.65	⋯	⋯	11.5	11.8 ± 0.6	5.44	5.45 ± 0.15	⋯	⋯
4859	He II	0.000	2.70[e]	2.70[e]	0.181[e]	0.181[e]	⋯	⋯	4.23[e]	4.23[e]	2.45[e]	2.45[e]	⋯	⋯
4861	Hβ	0.000	100.[e]	100. ± 0.[e]	100.[e]	100. ± 0.[e]	⋯	⋯	100.[e]	100. ± 0.[e]	100.[e]	100. ± 0.[e]	100.	100. ± 0.
4922	He I	−0.021	⋯	⋯	⋯	⋯	⋯	⋯	⋯	⋯	⋯	⋯	1.11	1.08 ± 0.11
4959	[O III]	−0.030	396.	383. ± 4.	351.	346. ± 4.	⋯	⋯	457.	442. ± 3.	369.	368. ± 2.	288.	277. ± 0.
5007	[O III]	−0.042	1201.	1147. ± 10.	1092.	1072. ± 11.	⋯	⋯	1380.	1318. ± 3.	1194.	1191. ± 5.	834.	791. ± 1.
5199	[N I]	−0.086	⋯	⋯	⋯	⋯	⋯	⋯	11.9	10.8 ± 0.6	⋯	⋯	0.615	0.551 ± 0.066
5234	[Fe VI]	−0.094	⋯	⋯	⋯	⋯	⋯	⋯	⋯	⋯	1.49	1.48 ± 0.39	⋯	⋯
5412	He II	−0.134	7.87	6.77 ± 0.52	⋯	⋯	⋯	⋯	10.0	8.64 ± 0.57	4.20	4.17 ± 0.35	0.413[a]	0.347 ± 0.043[a]
5518	[Cl III]	−0.157	⋯	⋯	⋯	⋯	⋯	⋯	⋯	⋯	⋯	⋯	0.237	0.194 ± 0.066
5538	[Cl III]	−0.161	⋯	⋯	⋯	⋯	⋯	⋯	⋯	⋯	⋯	⋯	0.864	0.702 ± 0.066
5755	[N II]	−0.207	⋯	⋯	⋯	⋯	⋯	⋯	12.2	9.72 ± 0.57	⋯	⋯	4.98	3.81 ± 0.19
5806	C IV	−0.217	⋯	⋯	⋯	⋯	⋯	⋯	⋯	⋯	⋯	⋯	34.7	26.2 ± 0.6
5876	He I	−0.231	11.3	8.76 ± 0.56	18.3	16.6 ± 0.6	⋯	⋯	12.8	9.89 ± 0.62	10.5	10.3 ± 0.3	26.1	19.4 ± 0.2
6300	[O I]	−0.313	5.09	3.58 ± 0.47	⋯	⋯	⋯	⋯	22.8	16.1 ± 0.8	⋯	⋯	5.33	3.55 ± 0.03
6311	He II	−0.315	0.276[e]	0.194[e]	⋯	⋯	⋯	⋯	0.430[e]	0.303[e]	⋯	⋯	⋯	⋯
6312	[S III]	−0.315	7.03[e]	4.94 ± 0.73[e]	⋯	⋯	⋯	⋯	1.64[e]	1.15 ± 0.28[e]	⋯	⋯	5.09	3.39 ± 0.03
6364	[O I]	−0.325	1.37	0.950 ± 0.527	⋯	⋯	⋯	⋯	6.87	4.79 ± 0.67	⋯	⋯	1.87	1.23 ± 0.07
6435	[Ar V]	−0.338	1.62	1.11 ± 0.16	⋯	⋯	⋯	⋯	⋯	⋯	⋯	⋯	⋯	⋯
6548	[N II]	−0.358	16.0	10.7 ± 0.2	⋯	⋯	⋯	⋯	283.	190. ± 1.	0.914	0.895 ± 0.318	63.3	39.9 ± 0.1
6560	He II	−0.360	10.9[e]	7.29[e]	0.585[e]	0.500[e]	⋯	⋯	16.9[e]	11.3[e]	6.85[e]	6.70[e]	⋯	⋯
6563	Hα	−0.360	418.[e]	279. ± 0.[e]	331.[e]	284. ± 1.[e]	⋯	⋯	414.[e]	278. ± 0.[e]	288.[e]	282. ± 0.[e]	455.	286. ± 0.
6584	[N II]	−0.364	51.8	34.5 ± 0.2	2.52	2.16 ± 0.41	⋯	⋯	868.	580. ± 2.	3.48	3.40 ± 0.32	198.	124. ± 0.
6678	He I	−0.380	6.57	4.30 ± 0.28	4.55	3.87 ± 0.35	⋯	⋯	4.51	2.96 ± 0.17	2.34	2.29 ± 0.14	7.57	4.63 ± 0.17

Table 3
(Continued)

Wave			IC 2165		IC 3568		NGC 2440 UV		NGC 2440 Opt		NGC 3242		NGC 5315	
(Å)	ID[c]	f(λ)	F(λ)	I(λ)	F(λ)	I(λ)	F(λ)	I(λ)	F(λ)	I(λ)	F(λ)	I(λ)	F(λ)	I(λ)
6716	[S II]	−0.387	3.23	2.09 ± 0.34	⋯	⋯	⋯	⋯	7.63	4.97 ± 0.51	⋯	⋯	3.94	2.39 ± 0.07
6731	[S II]	−0.389	4.22	2.73 ± 0.33	⋯	⋯	⋯	⋯	13.2	8.55 ± 0.51	⋯	⋯	7.81	4.73 ± 0.14
7006	[Ar V]	−0.433	2.59	1.59 ± 0.33	⋯	⋯	⋯	⋯	6.67	4.12 ± 0.40	⋯	⋯	⋯	⋯
7065	He I	−0.443	9.28	5.66 ± 0.38	5.57	4.60 ± 0.56	⋯	⋯	4.40	2.69 ± 0.55	4.23	4.11 ± 0.49	15.7	8.85 ± 0.11
7136	[Ar III]	−0.453	16.5	9.91 ± 0.32	8.36	6.88 ± 0.58	⋯	⋯	32.9	19.9 ± 0.3	7.17	6.97 ± 0.34	54.7	30.4 ± 0.12
7237	[Ar IV]	−0.468	⋯	⋯	⋯	⋯	⋯	⋯	⋯	⋯	⋯	⋯	0.728	0.397 ± 0.019
7281	He I	−0.475	⋯	⋯	⋯	⋯	⋯	⋯	⋯	⋯	⋯	⋯	1.21	0.653 ± 0.027
7324	[O II]	−0.481	7.44	4.35 ± 0.38	⋯	⋯	⋯	⋯	20.4	12.0 ± 0.6	⋯	⋯	20.5	11.0 ± 0.0
7751	[Ar III]	−0.539	6.53	3.57 ± 0.52	3.17	2.52 ± 0.84	⋯	⋯	8.68	4.78 ± 0.57	2.36	2.29 ± 0.52	15.2	7.55 ± 0.0
8046	[Cl IV]	−0.574	⋯	⋯	⋯	⋯	⋯	⋯	⋯	⋯	⋯	⋯	0.512	0.244 ± 0.049
8237	He II	−0.595	⋯	⋯	⋯	⋯	⋯	⋯	⋯	⋯	3.44	3.32 ± 0.68	⋯	⋯
8446	Pa 18 + O I + Pa 17	−0.616	⋯	⋯	⋯	⋯	⋯	⋯	4.51	2.28 ± 0.69	⋯	⋯	1.01	0.453 ± 0.042
8501	[Cl III] + P.16	−0.622	⋯	⋯	⋯	⋯	⋯	⋯	⋯	⋯	⋯	⋯	0.495	0.222 ± 0.023
8545	P 15	−0.626	⋯	⋯	⋯	⋯	⋯	⋯	⋯	⋯	⋯	⋯	0.669	0.298 ± 0.026
8598	Pa 14	−0.631	⋯	⋯	⋯	⋯	⋯	⋯	⋯	⋯	⋯	⋯	1.26	0.558 ± 0.034
8665	Pa 13	−0.637	⋯	⋯	⋯	⋯	⋯	⋯	⋯	⋯	⋯	⋯	1.21	0.530 ± 0.047
8750	Pa 12	−0.644	⋯	⋯	⋯	⋯	⋯	⋯	⋯	⋯	⋯	⋯	1.94	0.841 ± 0.046
8863	Pa 11	−0.654	⋯	⋯	⋯	⋯	⋯	⋯	⋯	⋯	⋯	⋯	2.58	1.11 ± 0.09
9015	P 10	−0.666	⋯	⋯	⋯	⋯	⋯	⋯	⋯	⋯	⋯	⋯	6.45	2.73 ± 0.17
9069	[S III]	−0.670	22.4	10.6 ± 0.2	⋯	⋯	⋯	⋯	20.7	9.84 ± 0.71	3.92	3.77 ± 0.80	123.	51.8 ± 0.17
9228	Pa 9	−0.610	4.48	2.26 ± 0.20	⋯	⋯	⋯	⋯	⋯	⋯	2.78	2.67 ± 0.33	5.35	2.43 ± 0.06
9532	[S III]	−0.632	52.8	26.0 ± 0.5	8.98	6.84 ± 1.52	⋯	⋯	56.5	28.0 ± 0.8	10.8	10.4 ± 0.8	316.	140. ± 0.
9546	Pa 8	−0.633	4.52	2.23 ± 0.46	⋯	⋯	⋯	⋯	⋯	⋯	⋯	⋯	⋯	⋯
10,050	Pa 7	−0.668	⋯	⋯	⋯	⋯	⋯	⋯	⋯	⋯	⋯	⋯	6.33	2.67 ± 0.14
c[f]			0.49		0.19		0.48		0.48		0.03		0.56	
Hα/Hβ[g]			2.79		2.83		2.78		2.78		2.82		2.86	
log $F_{H\beta}$[h]			−12.37		−12.84		−12.46[h]		−12.46		−12.07		−11.77	

[a] P Cyg profile; stellar line.
[b] P Cyg profile; stellar + nebular line contribution.
[c] Identifications ending in "fl" indicate fluorescence.
[d] Flux affected by possible artifact.
[e] Flux partitioned among multiple contributing emission lines: see text.
[f] Logarithmic extinction at Hβ.
[g] Expected intrinsic Hα/Hβ ratio at nebular temperature and density.
[h] Flux of Hβ λ4861 within extraction aperture in ergs cm^{-2} s^{-1}.

Table 4
Fluxes and Intensities II

Wave			NGC 5882		NGC 6537		NGC 6778		NGC 7662		PB6	
(Å)	ID[b]	f(λ)	F(λ)	I(λ)	F(λ)	I(λ)	F(λ)	I(λ)	F(λ)	I(λ)	F(λ)	I(λ)
1175	C III	1.849	0.508	2.46 ± 0.56	…	…	…	…	12.6	17.1 ± 1.2	2.81	9.72 ± 13.19
1241	N V	1.636	2.32[a]	9.35 ± 1.40[a]	…	…	…	…	2.42	3.17 ± 0.19	41.2	123. ± 136.
1247	C III	1.620	…	…	…	…	…	…	0.297	0.388 ± 0.050	…	…
1266	Fe II	1.569	…	…	…	…	…	…	1.04	1.35 ± 0.11	…	…
1305	O I	1.478	0.212	0.747 ± 0.278	…	…	…	…	…	…	130.	350. ± 356.
1336	C II	1.415	0.618[a]	2.06 ± 0.23[a]	…	…	1.07	11.8 ± 18.1	2.25	2.85 ± 0.18	…	…
1344	O IV + N II	1.400	0.253	0.835 ± 0.248	…	…	…	…	0.663	0.835 ± 0.125	…	
1370	O V	1.354	0.564[a]	1.79 ± 0.18[a]	…	…	…	…	…	…		
1394	Si IV	1.316	…	…	…	…	…	…	1.01	1.25 ± 0.14	…	…
1402	S IV] + O IV]?	1.307	…	…	…	…	…	…	13.1	16.3 ± 0.8	29.6	70.8 ± 65.38
1485	N IV]	1.231	<0.368	…	3.23	354. ± 28.	…	…	12.8	15.7 ± 0.7	86.4	196. ± 173
1549	C IV	1.184	2.66[a]	7.30 ± 0.53[a]	3.60	330. ± 58.	…	…	332.	403. ± 17.	586.	1288. ± 1100.
1575	[Ne V]	1.168	0.365	0.987 ± 0.231	…	…	…	…	4.00	4.84 ± 0.52	…	…
1602	[Ne IV]	1.153	…	…	…	…	…	…	2.18	2.64 ± 0.18	6.46	13.9 ± 12.78
1640	He II	1.136	11.0	29.1 ± 0.65	1.66	127. ± 12.	6.89	47.5 ± 6.6	236.	285. ± 12.	334.	711. ± 589.
1660	O III]	1.129	…	…	…	…	…	…	5.53	6.67 ± 0.99	4.55	9.64 ± 8.74
1666	O III]	1.128	…	…	…	…	…	…	14.8	17.8 ± 0.9	6.55	13.9 ± 11.98
1750	N III]	1.119	<1.64	<1.67	…	…	…	…	7.86	9.45 ± 1.02	…	…
1906	C III]	1.224	4.27	12.1 ± 4.17	…	…	…	…	167.	204. ± 9.	286.	647. ± 588
1909	C III]	1.229	5.19	14.8 ± 4.19	…	…	…	…	119.	146. ± 7.	135.	306. ± 314.
1981	[Fe VI]	1.357	…	…	…	…	…	…	1.94	2.43 ± 0.47	…	…
2187	He II + O III fl	1.653	…	…	…	…	…	…	1.22	1.60 ± 0.18	…	…
2214	He II	1.620	…	…	…	…	…	…	0.957	1.25 ± 0.19	…	…
2253	He II Pa 10–3	1.542	…	…	…	…	…	…	1.29	1.66 ± 0.18	…	…
2324	[O III]/C II]	1.359	1.22	3.90 ± 0.42	…	…	…	…	9.20	11.5 ± 0.6	28.9	71.7 ± 69.0
2385	He II Pa ϵ	1.204	…	…	…	…	…	…	2.75	3.35 ± 0.17	…	…
2423	[Ne IV]	1.118	…	…	…	…	…	…	5.75	6.92 ± 0.34	150.	315. ± 258.
2470	[O II]	1.025	0.633	1.52 ± 0.38	…	…	…	…	…	…	…	…
2511	He II Pa δ	0.955	…	…	…	…	…	…	5.70	6.67 ± 0.34	12.9	24.3 ± 20.43
2733	He II Pa γ	0.701	0.633	1.15 ± 0.29	…	…	…	…	10.0	11.2 ± 0.4	22.6	35.7 ± 21.77
2819	He I	0.632	…	…	…	…	…	…	1.34	1.49 ± 0.52	…	…
2837	O III fl	0.619	1.94	3.29 ± 0.30	…	…	…	…	10.8	11.9 ± 0.6	…	…
2945	He I	0.550	1.94[c]	3.10 ± 0.29[c]	…	…	…	…	1.11	1.21 ± 0.32	…	
3025	O III fl	0.506	1.89	2.91 ± 0.70	…	…	…	…	7.15	7.77 ± 0.45	14.3	19.9 ± 11.1
3048	O III fl	0.494	3.82	5.82 ± 0.62	…	…	…	…	17.3	18.8 ± 0.6	22.0	30.2 ± 15.6
3133	O III fl	0.454	16.3	24.0 ± 5.1	…	…	…	…	105.	113. ± 2.	…	…
3203	He II Pa β	0.424	…	…	…	…	…	…	17.3	18.5 ± 2.6	…	…
3295	O II	0.389	…	…	43.1	190. ± 47.	…	…	…	…	…	…
3308	O III fl	0.384	…	…	…	…	…	…	23.5	25.0 ± 1.2	…	…
3340	O III fl	0.373	…	…	…	…	…	…	19.4	20.6 ± 0.7	…	…
3346	[Ne V]	0.371	…	…	58.3	240. ± 72.	…	…	…	…	…	…
3426	[Ne V]	0.344	…	…	91.1	338. ± 25.	…	…	…	…	…	…
3448	He I/O III fl	0.337	11.5	15.3 ± 3.2	…	…	…	…	30.2	32.0 ± 2.1	…	…
3727	[O II]	0.292	10.5	13.5 ± 1.3	5.66	17.3 ± 9.1	…	…	10.9	11.4 ± 2.7	…	…
3757	O III fl	0.284	…	…	…	…	…	…	10.4	10.9 ± 3.1	…	…
3797	He II + H10	0.272	…	…	…	…	…	…	4.05	4.24 ± 0.48	…	…

Table 4
(Continued)

Wave (Å)	ID[b]	f(λ)	NGC 5882		NGC 6537		NGC 6778		NGC 7662		PB6	
			F(λ)	I(λ)	F(λ)	I(λ)	F(λ)	I(λ)	F(λ)	I(λ)	F(λ)	I(λ)
3835	He II + H9	0.262	5.19	6.49 ± 0.42	…	…	…	…	6.82	7.12 ± 0.55	…	…
3869	[Ne III]	0.252	70.1	87.0 ± 1.9	70.6	185. ± 10.	…	…	88.7	92.5 ± 1.1	…	…
3889	He I + H8	0.247	13.2	16.2 ± 1.9	…	…	…	…	16.6	17.2 ± 0.5	…	…
3968	[Ne III]	0.224	21.1[d]	25.6 ± 0.4[d]	20.6[d]	48.5 ± 8.3[d]	…	…	26.4[d]	27.4 ± 0.5[d]	…	
3970	Hε	0.224	13.2[d]	16.0[d]	7.13[d]	16.8[d]	…	…	16.0[d]	16.6[d]	…	…
4026	He I + He II	0.209	2.77	3.30 ± 0.43	…	…	…	…	2.97	3.07 ± 0.61	…	…
4071	[S II]	0.196	2.83	3.35 ± 0.57	15.0	31.8 ± 9.8	…	…		2.44	2.52 ± 0.60	…
4100	He II	0.188	8.47(−2)[d]	9.94(−2)[d]	0.494[d]	1.01[d]	0.147[d]	0.202[d]	0.796[d]	0.821[d]	…	…
4101	Hδ	0.188	22.0[d]	25.8 ± 0.6[d]	16.5[d]	33.8 ± 7.8[d]	33.3[d]	46.0 ± 13.1[d]	26.1[d]	27.0 ± 0.3[d]	…	…
4339	He II	0.124	0.159[d]	0.176[d]	1.11[d]	1.79[d]	0.294[d]	0.364[d]	1.42[d]	1.45[d]	4.21[d]	4.48[d]
4340	Hγ	0.124	37.6[d]	41.8 ± 0.6[d]	30.4[d]	48.8 ± 1.9[d]	44.8[d]	55.4 ± 10.4[d]	45.1[d]	46.1 ± 0.8[d]	41.5[d]	44.2 ± 28.4[d]
4363	[O III]	0.118	5.88	6.50 ± 0.42	18.4	28.9 ± 1.7	…	…	18.3	18.7 ± 0.8	59.6	63.2 ± 48.2
4472	He I	0.090	4.91	5.30 ± 0.53	7.44	10.5 ± 3.8	…	…	2.60	2.64 ± 0.45	…	…
4640	N III + O II	0.048	3.56	3.71 ± 0.34	7.67	9.20 ± 1.93	…	…	6.05	6.10 ± 0.55	…	…
4686	He II	0.036	7.40[c]	7.63 ± 0.24[c]	62.1	71.2 ± 1.4	18.6	19.8 ± 11.1	59.5	59.9 ± 0.4	170.	170. ± 47.
4711	He I + [Ar IV]	0.030	4.50	4.62 ± 0.30	12.1	13.5 ± 1.4	…	…	7.92	7.96 ± 0.49	…	…
4740	[Ar IV]	0.023	4.63	4.72 ± 0.29	23.4	25.6 ± 1.4	…	…	6.80	6.82 ± 0.46	…	…
4859	He II	0.000	0.366[d]	0.366[d]	3.65[d]	3.65[d]	0.784[d]	0.786[d]	2.98[d]	2.98[d]	9.23[d]	9.03[d]
4861	Hβ	0.000	100.[d]	100. ± 0.[d]	100.[d]	100. ± 0.[d]	100.[d]	100. ± 0.[d]	100.[d]	100. ± 0.[d]	100.[d]	97.9 ± 0.7[d]
4959	[O III]	−0.030	337.	328. ± 2.	431.	384. ± 5.	179.	171. ± 6	414.	412. ± 2	344.	330. ± 71.
5007	[O III]	−0.042	1107.	1068. ± 4.	1360.	1161. ± 13.	512.	478. ± 13.	1323.	1314. ± 4	1087.	1034. ± 189.
5412	He II	−0.134	1.84	1.65 ± 0.48	8.97	5.38 ± 0.86	…	…	5.33	5.22 ± 0.47	…	…
5755	[N II]	−0.207	…	…	73.3	33.3 ± 0.9	…	…	…	…	…	…
5876	He I	−0.231	17.0	14.0 ± 0.34	46.8	19.3 ± 1.4	38.6	26.1 ± 12.9	11.0	10.6 ± 0.9	…	…
6300	[O I]	−0.313	…	…	46.9	14.2 ± 0.4	…	…	…	…	…	…
6311	He II	−0.315	3.48(−2)[d]	2.66(−2)[d]	0.869[d]	0.261[d]	…	…	0.226[d]	0.215[d]	…	…
6312	[S III]	−0.315	2.73[c]	2.09 ± 0.34[d]	31.5[d]	9.46 ± 0.42[d]	…	…	1.02[d]	0.968 ± 0.329[d]	…	
6364	[O I]	−0.325	…	…	22.0	6.37 ± 0.55	…	…	…	…	…	…
6435	[Ar V]	−0.338	…	…	16.6	4.57 ± 0.42	…	…	…	…	…	…
6548	[N II]	−0.358	3.88	2.86 ± 0.13	602.	154. ± 0	90.5	49.4 ± 3.6	0.964	0.909 ± 0.123	160.	122. ± 49.
6560	He II	−0.360	1.39[d]	1.02[d]	38.3[d]	9.67[d]	4.58[d]	2.49[d]	8.59[d]	8.10[d]	30.2[d]	23.1[d]
6563	Hα	−0.360	389.[d]	286. ± 1.[d]	1093.[d]	276. ± 0.[d]	527.[d]	286. ± 0.[d]	297.[d]	280. ± 0.[d]	414.[d]	317. ± 1.[d]
6584	[N II]	−0.364	12.8	9.37 ± 0.17	1866.	465. ± 1.	284.	153. ± 2	4.03	3.80 ± 0.21	345.	263. ± 28.
6678	He I	−0.380	6.54	4.73 ± 0.22	24.6	5.77 ± 0.25	16.3	8.54 ± 0.14	4.56	4.29 ± 0.40	22.2	16.8 ± 6.50
6716	[S II]	−0.387	2.17	1.56 ± 0.38	25.8	5.90 ± 0.25	24.8	12.9 ± 4.9	…	…	…	…
6731	[S II]	−0.389	2.34	1.68 ± 0.28	53.8	12.2 ± 0.2	28.3	14.7 ± 2.3	…	…	…	…
7006	[Ar V]	−0.433	…	…	38.9	7.43 ± 0.45	…	…	…	…	…	…
7065	He I	−0.443	8.21	5.63 ± 0.12	40.9	7.56 ± 0.46	…	…	4.34	4.04 ± 0.87	…	…
7136	[Ar III]	−0.453	19.8	13.5 ± 0.1	187.	33.1 ± 0.4	23.6	11.0 ± 4.59	10.2	9.47 ± 0.56	40.8	29.3 ± 13.56
7170	[Ar IV] + [Fe II]	−0.458	…	…	14.4	2.50 ± 0.35	…	…	…	…	…	…
7324	[O II]	−0.481	4.31	2.86 ± 0.27	133.	21.3 ± 0.3	…	…	…	…	…	…
7531	[Cl IV]	−0.510	…	…	5.35	0.764 ± 0.196	…	…	…	…	…	…
7593	He II	−0.518	…	…	9.65	1.34 ± 0.26	…	…	…	…	…	…
7751	[Ar III]	−0.539	5.68	3.59 ± 0.20	59.2	7.58 ± 0.13	…	…	2.80	2.57 ± 0.86	…	…
8046	[Cl IV]	−0.574	…	…	14.9	1.67 ± 0.06	…	…	…	…	…	…

Table 4
(Continued)

Wave			NGC 5882		NGC 6537		NGC 6778		NGC 7662		PB6	
(Å)	ID[b]	f(λ)	F(λ)	I(λ)	F(λ)	I(λ)	F(λ)	I(λ)	F(λ)	I(λ)	F(λ)	I(λ)
8237	He II	–0.595	⋯	⋯	17.0	1.75 ± 0.22	⋯	⋯	⋯	⋯	⋯	⋯
8598	H Pa 14	–0.631	2.08	1.22 ± 0.58	⋯	⋯	⋯	⋯	⋯	⋯	⋯	⋯
9015	H Pa 10	–0.666	⋯	⋯	23.8	1.88 ± 0.30	⋯	⋯	2.97	2.66 ± 0.29	⋯	⋯
9069	[S III]	–0.670	24.9	14.1 ± 0.5	568.	44.0 ± 0.5	55.1	17.7 ± 4.26	11.4	10.2 ± 0.4	⋯	⋯
9228	H Pa 9	–0.610	4.12	2.45 ± 0.54	21.2	2.07 ± 0.19	⋯	⋯	2.80	2.54 ± 0.31	⋯	⋯
9532	[S III]	–0.632	53.4	31.1 ± 0.3	1438.	129. ± 1.	134.	45.9 ± 7.27	26.2	23.6 ± 1.1	114.	72.5 ± 24.4
9546	H Pa 8	–0.633	13.2	7.67 ± 0.55	52.5	4.68 ± 0.22	⋯	⋯	2.62	2.36 ± 0.11	⋯	⋯
10,050	H Pa 7	–0.668	⋯	⋯	55.6	4.33 ± 0.85	⋯	⋯	⋯	⋯	114.	72.5 ± 24.4
10,120	He II	–0.672	⋯	⋯	150.	11.5 ± 0.5	⋯	⋯	⋯	⋯	114.	72.5 ± 24.4
c[e]			0.37		1.66		0.74		0.07		0.30	
Hα/Hβ[f]			2.86		2.76		2.86		2.80		2.94	
log $F_{H\beta}$[g]			−12.33		−13.11		−13.51		−12.26		−13.70	

[a] P Cyg profile; stellar line.
[b] Identifications ending in "fl" indicate fluorescence.
[c] Flux affected by possible artifact.
[d] Flux partitioned among multiple contributing emission lines: see text.
[e] Logarithmic extinction at Hβ.
[f] Intrinsic Hα/Hβ ratio at nebular temperature and density.
[g] Flux of Hβ λ4861 within extraction aperture in ergs cm^{-2} s^{-1}.

Table 5
Unidentified Lines

Wavelength (Å)	Nebula
1256	NGC 3242
1273	NGC 2440
1281	NGC 3242
1288	NGC 2440
1296	NGC 2440, NGC 3242
1309	NGC 2440
1317	NGC 2440
1388	NGC 3242
1511	NGC 3242, NGC 7662
1591	NGC 3242
1981	NGC 3242
2280	NGC 3242
2932	NGC 2440
9346	NGC 6537

Our spectrograms for PB6 are also weakly exposed, but we are able to combine the UV emission lines with published spectra to confirm the very high enrichments of He, C, and N noted in the literature. Photoionization models of these eight PNs will be presented in a forthcoming paper.

We note again that our data are strictly co-spatial (except for NGC 2440), meaning that we are sampling the same region in each PN across the entire observed spectral range. The co-spatial results are thus free of any need for aperture size or placement corrections whose values can be difficult to calculate and whose effects on the final abundances almost impossible to assess. All calculated elemental abundances are listed in Table 8; we only discuss CNO abundances here. Table 9 shows our CNO abundances and those of various other authors with whom we compare below. All of our O abundances come from ICF calculations. We compare our summed values for C and N where available (for some PNs we had to exclude lines compromised by stellar emission, which we discuss in more detail below). We derived upper limits for key undetected ions and note their potential contribution. We also compare the abundances derived with the ICF values and comment on any discrepancies with the sums. Note that the ICF values for PNs where the value of T[N II] is assumed are particularly uncertain; however, our conclusions are based on the summed-ion results, which are unaffected by this uncertainty. As mentioned above, T[N II] is used only to calculate ionic abundances for singly ionized species, which are generally minor contributors to the total C and N abundances. Further, comparison of results using our default T[N II] of 10,300 K from Kaler (1986) with the recipe from Kingsburgh & Barlow (1994) yields insignificant differences in the contribution of N+ to the total N abundance.

In the following subsections where we compare our CNO abundances for each nebula in detail with those from other authors, it is worth noting at the outset the level of agreement among all authors for all nebulae, shown in Figure 5. Individual research groups are denoted with the same symbol, as they tend to use the same methodology, the same atomic parameters, and similar observing technique. The elements are differentiated by symbol color. The figure shows that the agreement among all authors for O abundance is generally good, within 30% for most cases. The agreement for C and N is much poorer, with many deviations approaching a factor of a few. In an exhaustive comparison of abundances derived for Magellanic Cloud PNs, Shaw et al. (2010) noted several reasons why abundances of the same object often differ from author to author. In some cases the differences in Figure 5 can be attributed to other authors' use of fluxes obtained with different apertures; for nebulae with significant ionization stratification such discrepancies are worrisome. Discrepancies can also arise from the use of different atomic parameters, different extinction constants, different techniques (e.g., the adoption of different T_e or N_e for different ions), or flawed observing techniques or data calibration. Note that discrepancies in any datum or derived parameter propagate downstream to the derivation of the final elemental abundances. This is a particular problem for abundances derived with ICF methods. In the comparisons below, we attempted to select data from the literature that represent the best available for these well-observed nebulae.

3.2.1. IC 2165

This object has a bright, angularly small (~7″) core and a faint, extended halo (Corradi et al. 2003). There is significant ionization stratification with position along the slit, with most of the emission from very low ionization species such as O^+, N^+, and S^+ located on the periphery (see Figure 1). Our ICF and summed ion abundances agree very well for both C (12% difference) and N (7% difference), indicating that the ICF method is doing a good job of accounting for ionization states that would be missed had only optical data been available. Kwitter et al. (2003) observed IC 2165 (optical only); their O/H value is within ~12% of ours. Their N/H value is ~60% larger than our N/H, due to their comparably greater ICF(N) stemming from a smaller derived O^+/H^+. They did not observe C.

Pottasch et al. (2004) reported abundances for IC 2165 derived from combining *IUE*, ground-based optical (primarily) from Hyung (1994), and *Infrared Space Observatory (ISO)* fluxes. Both the *IUE* and *ISO* apertures are larger than this nebula, but the ground-based data were averages from multiple observers, where some spectra were obtained through smaller apertures placed at different nebular locations. The optical slit spectra from Hyung (1994), which were only 4″ long, weighted the center of the nebular emission more heavily and hence missed much of the [O II] λ3727 and [N II] λ6583 emission. Their O abundance is very close to ours, but this is somewhat of a coincidence: they derived a much lower O^+ abundance because of a lower observed I(3727), but they derive a significant O^{+3} abundance from the IR 25.8 μm line. We observed O IV] UV emission, but we used ICF(O) to account for O^{+3} and higher ionization stages. Their N/H is ~17% less than ours, mostly because their I(6584) was much lower than ours. Finally, their C/H is ~50% more than our value, in spite of very similar intensities for the relevant emission lines: the discrepancy may come from either or both of different atomic parameters or their adoption of somewhat different T_e values.

Most recently, IC 2165 was observed by Bohigas et al. (2013) (optical only), who obtained optical echelle spectroscopy of the inner 22″ × 27″ region. The much narrower STIS slit, as shown in Figure 1, passes through the long axis of the nebula and does not sample as large a variety of environments. Comparing with their results derived by the "standard" method, our O abundance is 37% larger than theirs, due primarily to our higher O^+/H^+. Our value and their value for N^+/H^+ are within ~12%, but as a result of their larger ICF(N), our N/H abundance is only ~55% of theirs. Their C abundance, derived

Table 6
Temperatures and Densities

Parameter	Diagnostic	IC 2165	IC 3568	NGC 2440	NGC 3242	NGC 5315	NGC 5882	NGC 6537	NGC 6778	NGC 7662
T_e	[O III]	14,230 ± 162	10,970 ± 205	15,350 ± 311	11,940 ± 74	9561 ± 125	9872 ± 189	16,680 ± 513	10,000[a]	13,170 ± 226
	[N II]	10,300[a]	10,300[a]	10,180 ± 452	10,300[a]	12,860 ± 635	10,300[a]	22,560 ± 2501	10,300[a]	10,300[a]
	[O II]	21,500 ± 12,060	⋯	11,390 ± 3109	⋯	⋯	⋯	⋯	⋯	⋯
	[S III]	⋯	⋯	13,790 ± 2045[c]	⋯	9867 ± 159[c]	16,870 ± 2280[b]	20,570 ± 839[c]	⋯	13,260 ± 2628[b]
N_e	[S II]	1606 ± 1111	⋯	4580 ± 2365	⋯	8819 ± 2578	750 ± 818	13,240 ± 5124	919 ± 1331	⋯
	[Cl III]	⋯	⋯	⋯	⋯	60,130 ± 93,870	⋯	⋯	⋯	⋯
	[C III]	7987 ± 2472	3620 ± 6363	6362 ± 1816	3837 ± 1025	43,620 ± 11,210	29,490 ± 28,620	⋯	⋯	3288 ± 976

[a] Default value.
[b] Used 9069.
[c] Used 9532.

Table 7
Ionic Abundances[a]

Ion	IC 2165	IC 3568	NGC 2440	NGC 3242	NGC 5315	NGC 5882	NGC 7662
He^{+}(5876)	5.70 ± 0.57(−2)	0.114 ± 0.012	5.35 ± 0.46(−2)	6.88 ± 0.22(−2)	0.132 ± 0.002	0.103 ± 0.004	6.72 ± 0.63(−2)
He^{+2}(4686)	4.85 ± 0.10(−2)	3.42 ± 0.52(−3)	7.39 ± 0.06(−2)	4.58 ± 0.02(−2)	⋯	6.92 ± 0.22(−3)	5.47 ± 0.04(−2)
C^{+}(2325)	2.98 ± 0.20(−6)	7.55 ± 1.46(−7)	5.29 ± 0.17(−6)	6.51 ± 0.16(−7)	1.22 ± 0.05(−6)	3.41 ± 0.40(−7)	8.47 ± 0.47(−7)
C^{+2}(1909)	1.72 ± 0.13(−4)	1.55 ± 0.26(−4)	1.42 ± 0.16(−4)	1.65 ± 0.08(−4)	2.22 ± 0.27(−4)	7.83 ± 2.06(−5)	1.28 ± 0.14(−4)
C^{+2}(1907)	1.72 ± 0.13(−4)	1.55 ± 0.26(−4)	1.42 ± 0.16(−4)	1.65 ± 0.07(−4)	2.21 ± 0.27(−4)	7.82 ± 2.06(−5)	1.28 ± 0.14(−4)
C^{+2}(4267)	⋯	⋯	⋯	⋯	4.96 ± 1.32(−4)	⋯	⋯
C^{+2}(adopt)	1.72 ± 0.13(−4)	1.55 ± 0.26(−4)	1.42 ± 0.16(−4)	1.65 ± 0.08(−4)	2.31 ± 0.27(−4)	7.83 ± 2.06(−5)	1.28 ± 0.14(−4)
C^{+3}(1549)	1.42 ± 0.12(−4)	⋯	4.73 ± 0.63(−5)	2.46 ± 0.13(−5)	⋯	⋯	1.07 ± 0.14(−4)
icf(C)	2.07 ± 0.10	1.06 ± 0.02	3.25 ± 0.35	1.71 ± 0.03	1.05 ± 0.01	1.10 ± 0.01	1.86 ± 0.08
N^{+}(6584)	4.61 ± 0.10(−6)	3.92 ± 0.81(−7)	7.46 ± 0.80(−5)	5.72 ± 0.54(−7)	1.91 ± 0.17(−5)	1.81 ± 0.05(−6)	5.68 ± 0.35(−7)
N^{+}(6548)	4.22 ± 0.11(−6)	⋯	7.20 ± 0.77(−5)	4.42 ± 1.58(−7)	1.81 ± 0.16(−5)	1.62 ± 0.08(−6)	4.00 ± 0.55(−7)
N^{+}(5755)	⋯	⋯	7.46 ± 0.80(−5)	⋯	1.91 ± 0.17(−5)	⋯	⋯
N^{+}(adopt)	4.52 ± 0.09(−6)	3.92 ± 0.81(−7)	7.39 ± 0.79(−5)	5.45 ± 0.52(−7)	1.89 ± 0.17(−5)	1.76 ± 0.04(−6)	5.36 ± 0.31(−7)
N^{+2}(1751)	<1.0(−5)	<2.7(−5)	1.18 ± 0.14(−4)	3.07 ± 0.37(−5)	1.30 ± 0.32(−4)	<2.6(−5)	1.60 ± 0.25(−5)
N^{+3}(1485)	4.68 ± 0.41(−5)	<8.1(−6)	1.69 ± 0.24(−4)	4.12 ± 0.23(−5)	<1.2(−5)⋯	<8.8(−6)	2.79 ± 0.38(−5)
N^{+4}(1240)	3.44 ± 0.36(−5)	⋯	5.23 ± 0.85(−5)	8.48 ± 0.88(−6)	⋯	⋯	5.01 ± 0.81(−6)
icf(N)	17.7 ± 1.14	33.3 ± 18.96	8.91 ± 1.52	73.5 ± 19.09	20.4 ± 3.1	32.7 ± 7.29	76.4 ± 19.21
O^{+}(3727)	1.27 ± 0.20(−5)	8.85 ± 5.46(−6)	4.38 ± 1.50(−5)	5.42 ± 1.46(−6)	1.21 ± 0.33(−5)	5.34 ± 0.89(−6)	4.64 ± 1.20(−6)
O^{+}(7325)	2.75 ± 0.67(−5)	⋯	5.15 ± 0.70(−5)	⋯	2.32 ± 0.30(−5)	3.34 ± 1.10(−5)	⋯
O^{+}(adopt)	1.57 ± 0.09(−5)	8.85 ± 5.46(−6)	4.54 ± 1.26(−5)	5.42 ± 1.46(−6)	1.79 ± 0.30(−5)	1.35 ± 0.29(−5)	4.64 ± 1.20(−6)
O^{+2}(5007)	1.36 ± 0.05(−4)	2.82 ± 0.17(−4)	1.25 ± 0.07(−4)	2.40 ± 0.05(−4)	3.47 ± 0.17(−4)	4.11 ± 0.31(−4)	1.95 ± 0.10(−4)
O^{+2}(4959)	1.31 ± 0.04(−4)	2.63 ± 0.16(−4)	1.22 ± 0.07(−4)	2.14 ± 0.04(−4)	3.50 ± 0.17(−4)	3.65 ± 0.28(−4)	1.77 ± 0.09(−4)
O^{+2}(4363)	1.32 ± 0.05(−4)	2.82 ± 0.17(−4)	1.25 ± 0.07(−4)	2.40 ± 0.05(−4)	3.03 ± 0.17(−4)	3.66 ± 0.35(−4)	1.95 ± 0.10(−4)
O^{+2}(adopt)	1.34 ± 0.04(−4)	2.77 ± 0.17(−4)	1.24 ± 0.07(−4)	2.34 ± 0.05(−4)	3.47 ± 0.17(−4)	4.00 ± 0.30(−4)	1.91 ± 0.10(−4)
icf(O)	1.85 ± 0.09	1.03 ± 0.01	2.38 ± 0.12	1.67 ± 0.02	1.00 ± 0.00	1.07 ± 0.00	1.81 ± 0.08
Ne^{+2}(3869)	2.58 ± 0.11(−5)	5.58 ± 0.41(−5)	2.17 ± 0.15(−5)	4.99 ± 0.11(−5)	9.41 ± 0.51(−5)	9.37 ± 0.74(−5)	3.41 ± 0.20(−5)
Ne^{+3}(1602)	3.70 ± 0.46(−5)	⋯	4.13 ± 0.59(−5)	3.64 ± 0.55(−5)	⋯	⋯	3.20 ± 0.45(−5)
Ne^{+4}(1575)	8.76 ± 1.80(−6)	⋯	1.22 ± 0.17(−4)	2.78 ± 0.31(−5)	⋯	2.41 ± 1.08(−5)	1.17 ± 0.19(−5)
icf(Ne)	2.02 ± 0.11	1.06 ± 0.02	3.21 ± 0.40	1.70 ± 0.03	1.03 ± 0.01	1.08 ± 0.00	1.86 ± 0.08
S^{+}(6716)	9.82 ± 1.68(−8)	⋯	3.58 ± 1.00(−7)	⋯	3.06 ± 0.72(−7)	8.27 ± 1.38(−8)	⋯
S^{+}(6731)	9.57 ± 1.65(−8)	⋯	3.50 ± 1.00(−7)	⋯	3.08 ± 0.72(−7)	8.29 ± 1.39(−8)	⋯
S^{+}(adopt)	9.68 ± 1.65(−8)	⋯	3.53 ± 0.99(−7)	⋯	3.08 ± 0.72(−7)	8.28 ± 1.39(−8)	⋯
S^{+2}(9069)	7.29 ± 0.22(−7)	3.13 ± 0.71(−7)	7.25 ± 0.83(−7)[b]	4.06 ± 0.33(−7)	8.36 ± 0.32(−6)[b]	1.99 ± 0.14(−6)	8.17 ± 1.30(−7)[b]
icf(S)	1.55 ± 0.05	1.76 ± 0.33	1.30 ± 0.05	2.44 ± 0.32	1.70 ± 0.14	2.59 ± 0.25	2.48 ± 0.32
Cl^{+2}(5517)	⋯	⋯	⋯	⋯	1.08 ± 0.43(−7)[b]	⋯	⋯
Cl^{+2}(5537)	⋯	⋯	⋯	⋯	1.18 ± 0.18(−7)[b]	⋯	⋯
Cl^{+2}(adopt)	⋯	⋯	⋯	⋯	1.16 ± 0.20(−7)	⋯	⋯
Cl^{+3}(8045)	⋯	⋯	⋯	⋯	2.12 ± 0.43(−8)	⋯	⋯
icf(Cl)	⋯	⋯	⋯	⋯	1.00 ± 0.00	⋯	⋯
Ar^{+2}(7135)	4.28 ± 0.18(−7)	5.26 ± 0.49(−7)	7.35 ± 0.33(−7)	4.43 ± 0.22(−7)	3.16 ± 0.10(−6)	1.30 ± 0.06(−6)	4.84 ± 0.35(−7)
Ar^{+2}(7751)	6.40 ± 0.94(−7)	7.98 ± 2.68(−7)	7.31 ± 0.93(−7)	6.02 ± 1.36(−7)	3.25 ± 0.10(−6)	1.44 ± 0.11(−6)	5.44 ± 1.83(−7)
Ar^{+2}(adopt)	4.88 ± 0.36(−7)	6.01 ± 0.98(−7)	7.34 ± 0.37(−7)	4.82 ± 0.43(−7)	3.18 ± 0.10(−6)	1.33 ± 0.06(−6)	4.97 ± 0.52(−7)
Ar^{+3}(4740)	5.44 ± 0.66(−7)	3.90 ± 1.16(−7)	6.92 ± 0.53(−7)	6.27 ± 0.25(−7)	⋯	7.34 ± 0.64(−7)	6.21 ± 0.52(−7)
Ar^{+4}(7005)	1.39 ± 0.29(−7)	⋯	3.00 ± 0.33(−7)	⋯	⋯	⋯	⋯
Ar^{+4}(6435)	2.08 ± 0.31(−7)	⋯	⋯	⋯	⋯	⋯	⋯
Ar^{+4}(adopt)	1.66 ± 0.21(−7)	⋯	3.00 ± 0.33(−7)	⋯	⋯	⋯	⋯
icf(Ar)	1.96 ± 0.09	1.06 ± 0.02	2.69 ± 0.17	1.69 ± 0.02	1.05 ± 0.03	1.10 ± 0.01	1.84 ± 0.08

[a] Abundances relative to H^{+}; nn.n(−k) = nn.n × 10^{-k}.
[b] Derived using Te[S III].

Table 8
Total Elemental Abundances[a]

Parameter	IC 2165	IC 3568	NGC 2440	NGC 3242	NGC 5315	NGC 5882	NGC 7662	Solar	Orion
He/H	0.106 ± 0.006	0.118 ± 0.012	0.127 ± 0.005	0.115 ± 0.002	0.132 ± 0.002	0.110 ± 0.004	0.122 ± 0.006	8.50(−2)	9.70(−2)
C/H (ICF)	3.56 ± 0.33(−4)	1.65 ± 0.30(−4)	4.61 ± 0.73(−4)	2.82 ± 0.14(−4)	2.43 ± 0.28(−4)	8.63 ± 2.26(−5)	2.38 ± 0.28(−4)	2.69(−4)	3.31(−4)
C/H (sum)	3.17 ± 0.18(−4)	1.56 ± 0.26(−4)	1.95 ± 0.17(−4)	1.90 ± 0.08(−4)	2.34 ± 0.27(−4)	7.86 ± 2.06(−5)	2.36 ± 0.20(−4)	2.69(−4)	3.31(−4)
C/O (ICF)	1.28 ± 0.06	5.59 ± 0.66(−1)	1.14 ± 0.07	7.07 ± 0.19(−1)	6.65 ± 0.57(−1)	1.95 ± 0.46(−1)	6.70 ± 0.45(−1)	5.50(−1)	6.16(−1)
C/O (sum)	1.14 ± 0.09	5.29 ± 0.96(−1)	0.48 ± 0.07	4.77 ± 0.23(−1)	0.64 ± 0.08	1.78 ± 0.49(−1)	6.70 ± 0.45(−1)	5.50(−1)	6.16(−1)
N/H (ICF)	8.01 ± 0.61(−5)	1.31 ± 0.69(−5)	6.59 ± 0.55(−4)	4.00 ± 1.09(−5)	3.86 ± 0.30(−4)	5.76 ± 1.35(−5)	4.34 ± 1.18(−5)	6.76(−5)	5.37(−5)
N/H (sum)	8.57 ± 0.54(−5)	<3.58(−5)	4.13 ± 0.26(−4)	8.09 ± 0.44(−5)	1.49 ± 0.32(−4)	<3.67(−5)	4.95 ± 0.46(−5)	6.76(−5)	5.37(−5)
N/O (ICF)	2.89 ± 0.15(−1)	4.44 ± 2.54(−2)	1.63 ± 0.28	1.00 ± 0.28(−1)	1.06 ± 0.08	1.30 ± 0.29(−1)	1.22 ± 0.34(−1)	1.38(−1)	1.00(−1)
N/O (sum)	3.08 ± 0.27(−1)	<1.21(−1)	1.02 ± 0.14	2.03 ± 0.12(−1)	0.41 ± 0.09	<8.30(−2)	1.40 ± 0.16(−1)	1.38(−1)	1.00(−1)
O/H	2.78 ± 0.17(−4)	2.95 ± 0.21(−4)	4.04 ± 0.50(−4)	3.98 ± 0.10(−4)	3.65 ± 0.18(−4)	4.42 ± 0.33(−4)	3.54 ± 0.23(−4)	4.89(−4)	5.37(−4)
Ne/H	5.21 ± 0.39(−5)	5.93 ± 0.49(−5)	6.98 ± 1.00(−5)	8.50 ± 0.24(−5)	9.74 ± 0.54(−5)	1.01 ± 0.08(−4)	6.34 ± 0.44(−5)	8.51(−5)	1.12(−4)
Ne/O	1.88 ± 0.05(−1)	2.01 ± 0.04(−1)	1.73 ± 0.06(−1)	2.13 ± 0.01(−1)	2.67 ± 0.05(−1)	2.29 ± 0.12(−1)	1.79 ± 0.02(−1)	1.74(−1)	2.09(−1)
S/H	1.28 ± 0.05(−6)	5.51 ± 1.64(−7)	1.40 ± 0.14(−6)	9.88 ± 1.53(−7)	1.47 ± 0.12(−5)	5.37 ± 0.69(−6)	2.03 ± 0.42(−6)	1.32(−5)	1.66(−5)
S/O	4.61 ± 0.29(−3)	1.87 ± 0.61(−3)	3.47 ± 0.35(−3)	2.48 ± 0.40(−3)	4.03 ± 0.38(−2)	1.22 ± 0.11(−2)	5.72 ± 1.21(−3)	2.70(−2)	3.09(−2)
Cl/H	…	…	…	…	1.16 ± 0.20(−7)	…	…	3.16(−7)	2.88(−7)
Cl/O	…	…	…	…	3.16 ± 0.52(−4)	…	…	6.46(−4)	5.36(−4)
Ar/H	2.35 ± 0.19(−6)	1.05 ± 0.15(−6)	4.64 ± 0.38(−6)	1.87 ± 0.09(−6)	3.34 ± 0.11(−6)	2.28 ± 0.12(−6)	2.06 ± 0.16(−6)	2.51(−6)	4.17(−6)
Ar/O	8.47 ± 0.54(−3)	3.57 ± 0.58(−3)	1.15 ± 0.07(−2)	4.70 ± 0.22(−3)	9.16 ± 0.20(−3)	5.15 ± 0.30(−3)	5.81 ± 0.35(−3)	5.13(−3)	7.77(−3)

[a] Abundances relative to H; nn.n(−k) = nn.n × 10^{-k}.

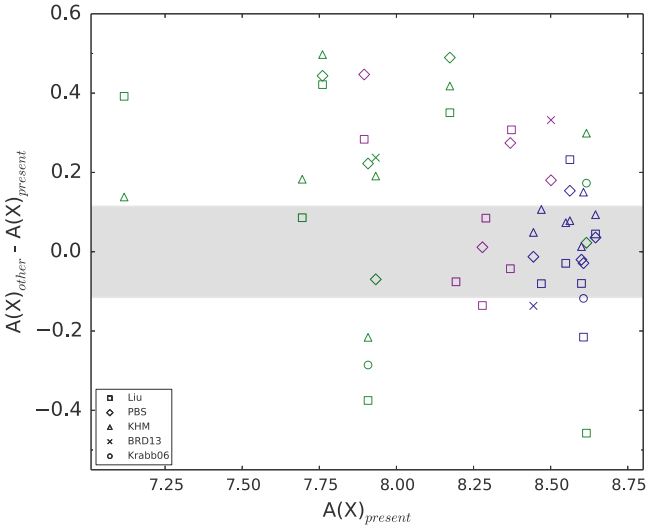

Figure 5. Difference between published log abundances and those of this study, as a function of our log abundance for the elements. Elements X are color-coded C: *magenta*, N: *green*, and O: *blue*. Published abundances are from Liu and collaborators (*squares*): Liu et al. (2004a, 2004b), Tsamis et al. (2003); Pottasch and collaborators (*diamonds*): Pottasch et al. (2002), Bernard-Salas et al. (2002), Pottasch & Bernard-Salas (2008), Pottasch et al. (2004), Bohigas et al. (2013); Kwitter and collaborators (*triangles*): Milingo et al. (2002), Kwitter et al. (2003), Henry et al. (2004), Milingo et al. (2010); Dufour and collaborators (*stars*): Bohigas et al. (2013); and Krabb (*circles*): Krabbe & Copetti (2006). Gray band shows agreement within 30%.

exclusively from permitted lines, is almost double ours. The He abundance (He/H = 0.106), coupled with low N/O (∼0.3), corroborates the conclusion that IC 2165 originates from a progenitor not much more massive than $\sim 2\,M_{\odot}$ (e.g., Bohigas et al. 2013). The C/O ratio (∼1.2) is larger than the solar value, perhaps indicative of some C production.

3.2.2. IC 3568

This object is ∼18″ in size, with a bright inner core of ∼7″; there is little ionization stratification; however, the FUV spectrum shows stellar P Cyg profiles in N V and C IV. Our calculations of ICF and summed-ion abundances for C agree to within 6%, giving confidence in the numbers. Many of our spectrograms for this object were less than optimally exposed: we determined only upper limits for nebular UV N lines, for example. Henry et al. (2004) derived abundances for IC 3568 from optical spectra; their N/H and O/H are 37% and 28% higher, respectively. Liu et al. (2004a, 2004b) also observed IC 3568 and calculated CNO abundances combining *IUE* and *ISO* data with optical recombination lines and with collisionally excited lines. We compare our results with their collisionally excited line results and find that the C/H and O/H agree within 25%. However, our N/H using ICF(N) is only 40% of theirs, despite our N^+/H^+ being twice as large. The difference is due to their inclusion of N III] λ1750 from *IUE* data (we have only upper limits from our STIS data) to derive N^{++}/H^+. We detected only the N^+ ion, which had a rather large ICF(N) of 33.3, but our sum of N^+ and the upper limit to N^{+2} agrees well

Table 9
Abundance Comparison[a]

Nebula	C	N	O	Reference
IC 2165	3.17(−4)	8.57(−5)	2.78(−4)	This paper
	6.81(−4)	1.48(−4)	2.03(−4)	Bohigas et al. (2013)
	4.80(−4)	7.30(−5)	2.70(−4)	Pottasch et al. (2004)
	⋯	1.33(−4)	3.11(−4)	Kwitter et al. (2003)
IC 3568	1.56(−4)	1.31(−5)[b]	2.95(−4)	This paper
	1.31(−4)	3.23(−5)	2.45(−4)	Liu et al. (2004a, 2004b)
	⋯	1.80(−5)	3.77(−4)	Henry et al. (2004)
NGC 2440	1.95(−4)	4.13(−4)	4.04(−4)	This paper
	⋯	6.15(−4)	3.08(−4)	Krabbe & Copetti (2006)
	2.37(−4)	1.44(−4)	2.46(−4)	Tsamis et al. (2003)
	6.34(−4)	8.22(−4)	5.71(−4)	Kwitter et al. (2003)
	7.19(−4)	4.35(−4)	3.78(−4)	Bernard-Salas et al. (2002)
NGC 3242	1.90(−4)	8.09(−5)	3.98(−4)	This paper
	1.95(−4)	1.35(−4)	3.80(−4)	Pottasch & Bernard-Salas (2008)
	⋯	4.19(−5)	3.09(−4)	Krabbe & Copetti (2006)
	1.39(−4)	3.41(−5)	3.31(−4)	Tsamis et al. (2003)
	⋯	4.92(−5)	4.10(−4)	Milingo et al. (2002)
NGC 5315	2.34(−4)	1.49(−4)	3.65(−4)	This paper
	⋯	3.90(−4)	4.37(−4)	Milingo et al. (2010)
	2.12(−4)	3.34(−4)	6.23(−4)	Tsamis et al. (2003)
	4.40(−4)	4.60(−4)	5.20(−4)	Pottasch et al. (2002)
NGC 5882	7.86(−5)	5.76(−5)[b]	4.42(−4)	This paper
	1.51(−4)	1.52(−4)	4.90(−4)	Tsamis et al. (2003)
	⋯	1.81(−4)	5.48(−4)	Kwitter et al. (2003)
	2.20(−4)	1.60(−4)	4.80(−4)	Pottasch et al. (2004)
NGC 7662	2.36(−4)	4.95(−5)	3.54(−4)	This paper
	4.79(−4)	6.03(−5)	3.31(−4)	Liu et al. (2004a, 2004b)
	⋯	7.54(−5)	4.19(−4)	Kwitter et al. (2003)

[a] Abundances relative to H; nn.n(−k) = = nn.n × 10^{-k}.
[b] ICF value; only N^+ available.

with that of Liu et al. (2004a, 2004b). Our O abundance agrees within ~25% to that of Henry et al. (2004). Based on our results, He/H (0.118) is slightly above solar, C/O (~0.5) is solar, and N/O (0.04) is slightly sub-solar.

3.2.3. NGC 2440

This object is angularly large (74″ × 42″) with highly stratified ionization. Our results for NGC 2440 are uncertain to the extent that the slit positions for the UV and optical observations sampled different locations (see Section 2.3). Based on the STIS data, the ICF abundances of C and N are 60% higher and 2.3 times higher than the ion-sum values, respectively. Both O^{+} and O^{++} are well measured in our spectra, as are He^{+} and He^{++}, so the ICF values should be accurate. It may be that the spatial offset of the UV and optical spectra, described above, sampled sufficiently different regions that these two results are not directly comparable.

NGC 2440 has been observed by many authors, including Bernard-Salas et al. (2002), who combined *ISO* IR data with *IUE* UV data and previously published optical data, and Tsamis et al. (2003), who observed the entire nebula and combined their optical data with *IUE* data; Kwitter et al. (2003) and Krabbe & Copetti (2006) observed in the optical only. Our ion-summed C abundance is 82% of what Tsamis et al. (2003) reports and only 28% of values reported by Kwitter et al. (2003) and Bernard-Salas et al. (2002). Our ion-summed N abundance is ~50% of that found by Kwitter et al. (2003), ~68% of that by Krabbe & Copetti (2006), and ~95% of the value from Bernard-Salas et al. (2002), but 2.8 times that of Tsamis et al. (2003). These last authors did not detect any N^{+}, so their entire N abundance is based on *IUE* lines. Inspection of their ionic abundances reveals that their values of N^{++}, N^{+3}, and N^{+4} are systematically 2–5 times lower than ours. The source of the discrepancy may lie in our mis-matched apertures. However, since this nebula is larger than the *ISO* and *IUE* apertures and is highly stratified, the discrepancy could equally well indicate a problem with matching the satellite data to those from the ground-based spectra. The He/H ratio in NGC 2440 (0.127) and the N/O ratio, whether ICF (1.6) or summed-ion (1.0), are both greater than solar and suggest that the progenitor of this PN was relatively high mass.

3.2.4. NGC 3242

This object is angularly large, with a core of 16″ × 26″, surrounded by a faint shell of about 40″ × 35″ (Corradi et al. 2003). Within the bright inner core there is moderate ionization stratification. Our ICF and summed-ion results for NGC 3242 are quite disparate: $C(ICF) = 1.5 \times C(sum)$ and $N(ICF) = 0.5 \times N(sum)$. Milingo et al. (2002) observed NGC 3242 in the optical only, as did Krabbe & Copetti (2006). Pottasch & Bernard-Salas (2008) combined *ISO* IR data with *IUE* UV data and previously published ground-based optical data. Tsamis et al. (2003) observed the entire nebula and combined their data with *IUE* data.

All of these authors' O abundances agree with ours to ~30%. The C abundance from Tsamis et al. (2003) is half of our ICF value and 73% of our summed-ion value; they used only C III] λ1909 and did not include C IV λ1549 or C II] λ2324. The C abundance (and also the C^{+2} and C^{+3} ionic abundances) from Pottasch & Bernard-Salas (2008) agrees perfectly with our summed-ion value in spite of significantly different intensities for the lines used to derive the ionic abundances. Their C abundance is 70% of our ICF value. Our ICF-based N abundance agrees to ~20% with those of Krabbe & Copetti (2006), Tsamis et al. (2003), and Milingo et al. (2002), but is three times lower than that of Pottasch & Bernard-Salas (2008). Since our summed-ion N value is twice as high as the ICF value, the agreement just described suffers by a factor of two. The He/H ratio in NGC 3242 is slightly above solar (0.115); the N/O is 0.1 (ICF) or 0.2 (sum).

3.2.5. NGC 5315

This object is angularly small (~15″), with modest ionization stratification, but there are very bright stellar emission lines. This analysis for this PN is problematic: the S/N is not as high as needed for a robust abundance analysis, since we had to avoid much of the spatial extent of the nebula in order to exclude a substantial contribution of scattered stellar P Cyg emission to the nebular emission. As a result, we have not used any He II lines in the abundance analysis; the ICF values in Table 7 should therefore be viewed as lower limits. NGC 5315 was observed previously in the optical by Milingo et al. (2010) and by Tsamis et al. (2003), who observed the entire nebula and combined their data with *IUE* data; Pottasch et al. (2002) combined their IR observations with *IUE* and previously published optical data. These other investigators derived O abundances ~18%–70% larger than ours. Their N abundances are within 30% of our N(ICF) values and 2–3 times our summed-ion N abundance. Our ICF and summed-ion C abundances are in excellent agreement and within ~10% of the Tsamis et al. (2003) value. Despite Pottasch et al. (2002) deriving ionic abundances for C^{+} and C^{++} similar to ours, their application of an ICF yields a C abundance roughly twice ours. Milingo et al. (2010), using only the C^{++} permitted line at λ4267, derive a C abundance 3.5 times ours. The He/H ratio (0.132) and the N/O ratio (1.1, using the ICF value) are clearly greater than the solar values.

3.2.6. NGC 5882

This nebula is intermediate in size (Corradi et al. 2000) with a bright, elliptical inner shell (11″ × 6″), surrounded by a spherical outer shell (15″); it has substantial ionization stratification. Scattered stellar light was an issue in the STIS observations, reducing the region of the slit usable for nebular analysis, with the higher-ionization lines of N and C being of stellar origin. NGC 5882 was observed in the optical by Kwitter et al. (2003) and by Tsamis et al. (2003), who observed the entire nebula and combined their data with *IUE* data. Pottasch et al. (2004) observed the full spatial extent of the nebula with *ISO* in the IR and combined their observations with *IUE* data in the UV and previously published, ground-based optical data (primarily from Tsamis et al. 2003). All of the O abundances agree with ours to 25%. The N abundances from these authors agree with each other to 20% but are 2–3 times ours, which is based solely on optical N^{+}/H^{+} and an ICF (N) of ~33. Our upper limit to the N III] λ1750 emission is less than half that of Pottasch et al. (2004), but their N^{+2} abundance (the dominant ionization stage), derived from the 57 μm emission line, is larger than ours by a factor of 5.

Tsamis et al. (2003) and Pottasch et al. (2004) derived C abundances from C III] λ1909 in the same *IUE* data, calculating similar C^{++}/H^{+} ratios, about twice what we derive from the co-

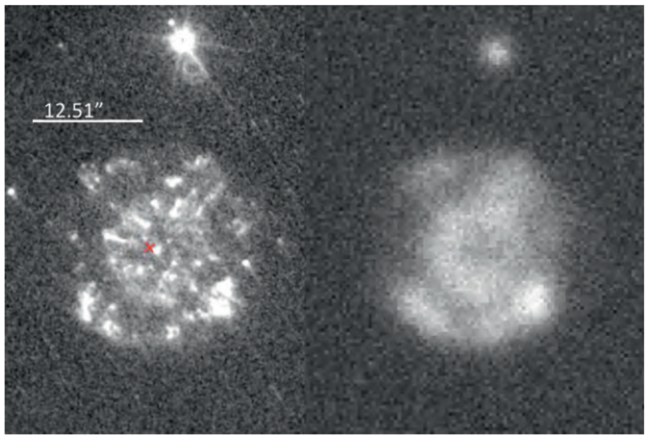

Figure 6. Images of PB 6 obtained with STIS in white light through the F28X50LP aperture (*left*), where the emission is dominated by Hα and [N II], compared to a ground-based image in [O III] λ5007 obtained by one of us (R.L.M.C.) with the EFOSC2 camera on the 3.5 m NTT ESO telescope under 1.″5 seeing conditions. The images are oriented with north up and east to the left; the bar in the upper left provides the scale. Note that the apparent double-shell structure in the NTT image is resolved into a complex set of knots in the higher-resolution STIS image.

spatial STIS data. This, together with the use of different ICF values, produces total C abundances that are 75% larger and 2.5 times larger than ours, respectively. The He/H (0.11) and N/O (0.13) in NGC 5882 are roughly solar.

3.2.7. NGC 7662

This nebula is moderately large, with a bright shell ∼30″ in diameter (Corradi et al. 2003) and considerable ionization stratification. Our STIS data show that the ICF values and summed-ion values agree very well, within ∼1% for C and ∼14% for N, indicating that, as in IC 2165, the ICF method is yielding reliable abundances. NGC 7662 has been observed by Kwitter et al. (2003) in the optical and by Liu et al. (2004a, 2004b), who combined their data with *IUE* UV data. The O abundances agree well, within 20%. Our C abundance is only half that found by Liu et al. (2004a, 2004b), despite our ionic abundances agreeing with theirs to within 30%. The difference is that they apply an ICF (= 2.0) to their ion sum. Our N abundance is ∼65% of those derived by Liu et al. (2004a, 2004b) and Kwitter et al. (2003). The difference with Liu et al. (2004a, 2004b) appears mainly to be their higher N^{+4} because of a higher observed N V λ1240 emission, which is likely the result of scaling the fluxes from the *IUE* large aperture to their 1″ optical slit. Our ICF N abundance hinges on weak O^{+}/H^{+}, but the good agreement with the ion sum implies that the ICF itself is not the reason. The He/H (0.122) is higher than solar, but the N/O ratio (0.13) is very close to solar.

3.2.8. PB 6

This object is a small (14.″0 × 12.″5), clumpy nebula with a bright, [WC] central star, as shown in Figure 6. A ground-based image in [O III] obtained by one of us (R.L.M.C.; included in Figure 6) shows what appear to be two concentric, nearly circular shells, but the higher-resolution STIS image resolves the structure into a complex of knots. Some of the knots appear to have a linear or cometary structure oriented away from the central star, not unlike those seen in Abell 30 and Abell 78 (Fang et al. 2014). The He/H, C/O, and N/O ratios for this nebula have been reported to be extraordinarily high. Kaler et al. (1991) first noted the presence of very strong O VI emission in the optical, and strong stellar emission is apparent in our UV and optical spectrograms as well.

Our spectrograms are too weakly exposed to derive robust abundances, or even reliable physical diagnostics. García-Rojas et al. (2009, hereafter GRPP) obtained deep optical spectra in order to use faint recombination lines to derive abundances. They derived values for T_e and N_e from CELs that are consistent with other published values and found from ORLs high enrichments of He, C, and N. Our emission-line intensities, uncertain as they are, are consistent with those reported in GRPP apart from our detection of a stronger [N II] λ6583 flux. Our spectrograms, and the two zones within PB 6 analyzed by GRPP, indicate that the ionization is not strongly stratified within this nebula. We used the optical intensities from GRPP and our UV data to compute the abundances from CELs using ELSA, in order to compare techniques (in spite of the mis-matched apertures). We find that the He and CNO abundances derived in this way generally agree with those from GRPP, although the strong observed (but uncertain) C^{+3} abundance from our UV spectrum suggests that C could be even higher. Keller et al. (2014) modeled the central star spectrum to derive $T_{\rm eff}$ = 165,000 K and $\log(L/L_{\odot})$ = 3.43, using data from *FUSE* and our UV spectrograms from STIS; their results are also consistent with the high ionization of this nebula.

4. DISCUSSION

It is well known that PNs exhibit a wide variety of ionization structures. This is especially true of PNs that are not fully ionized, where the ionization is often a complicated function of position within the nebula. Unless spectra can be obtained that intercept the light from the full spatial extent of the nebula (which is usually achieved only for angularly small PNs, such as those in external galaxies), the derivation of nebular conditions and elemental abundances must of necessity sample a limited, possibly small volume within the nebulosity. We have shown here (as many before us have) that the most reliable elemental abundances are derived by observing a full range of ionic species, which requires spectra spanning at least the UV through optical bands, at high S/N and moderate to high spectral resolution. Often this requires the use of multiple spectrographs on different platforms. We believe that the most accurate abundances are derived when all spectroscopic apertures sample identical three-dimensional volumes of the nebulosity. Indeed, for nebulae with stratified ionization, co-spatial apertures are essential for deriving consistent plasma diagnostics, ICFs, and elemental abundances. We have shown in some key cases (including IC 2165, NGC 3242, and NGC 5882) that the primary reason for the large difference between our derived ionic and elemental abundances and those in the literature (up to a factor of a few; see Figure 5) is the mis-application of data from spatially distinct regions. It is our assertion, to be explored further in forthcoming papers, that to reach the level of precision necessary to discriminate between modern, competing theories of elemental yields in post-AGB stars, it simply will not suffice to scale or select emission-line intensities from one nebular region and transplant them to another, spatially distinct region.

Figure 7 graphically displays the summed abundance results given in Table 8 for the program PNs discussed in the previous

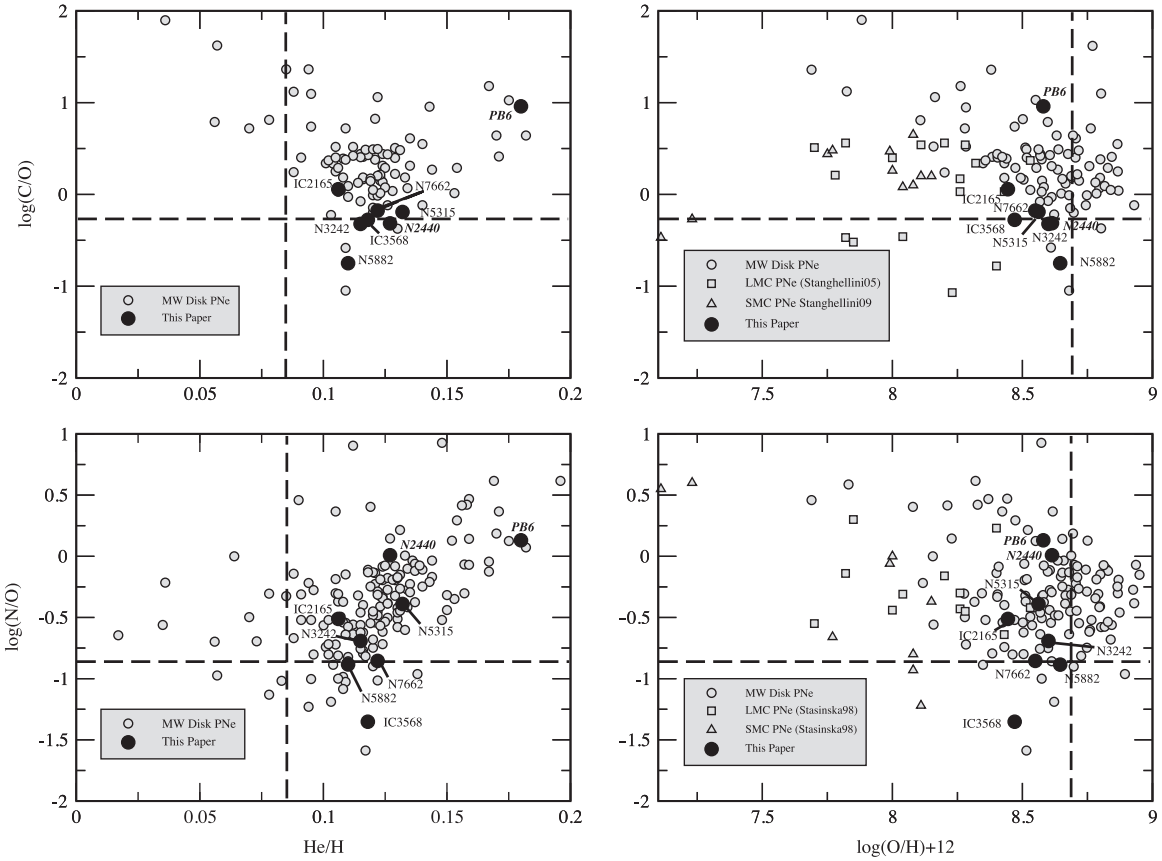

Figure 7. Left panels: log(C/O) and log(N/O) vs. He/H, respectively. Program objects are represented by large filled circles, while data from the KH database are indicated with small gray circles. Right panels: same as left panels but with log(O/H)+12 as the independent variable. Additional data for the LMC and SMC have also been included from papers cited in the legends. Bold dashed lines indicate solar values. Program objects are identified in each panel, where names of Type I PNs appear in italics. Note that the abundances for PB 6 are taken from GRPP.

section (large filled circles). Because our optical line measurements for PB6 proved to be unreliable (see Section 3.2), the positions for PB 6 in all four panels were determined using abundances from Peña et al. (1998). Despite the fact that our data for PB6 are less than satisfactory, we decided to include it in Figure 7 because it harbors a [WC] central star, it is a Type I PN, and it possesses an inordinately high nebular He abundance, making it an interesting object to compare with the other sample members. The left panels show log(C/O) and log (N/O) versus He/H, while the right panels do so for the same dependent variables against log(O/H)+12. To provide a comparison with a larger sample, the small gray dots show abundance ratios from the KH database. In the right panels we have also added results from Stanghellini et al. (2005, 2009) and Stasińska et al. (1998) for the LMC and SMC in order to extend the metallicity range to lower values. Within our sample of eight PNs, Type I objects are identified with italicized font, while names of non-Type I PNs are shown with regular font. The bold dashed lines show solar values from Asplund et al. (2009).

The right panels demonstrate that there is no clear trend in either C/O or N/O with respect to the metallicity range of objects observed, as gauged by log(O/H)+12. This is in contrast to what is anticipated by recent model results. Post-AGB stellar models and the consequent PN abundance predictions published by Karakas (2010) for low stellar metallicity progenitor stars (e.g., 0.004 (SMC), 0.008 (LMC), corresponding respectively to 8.00 and 8.30 on the horizontal scale) with birth masses below 4 $M_{\odot}$ suggest that C/O should be noticeably greater than in the case of the solar-like metallicities characteristic of our program objects. Similarly, above this mass threshold, where hot bottom burning (HBB) converts dredged-up C into primary N, N/O should be greater at low metallicities than at levels closer to solar. HBB most likely occurred during the late evolutionary stages of progenitors of IC 2165, NGC 2440, NGC 5315, and PB6 since their N/O ratios are significantly higher than those of the remaining sample PNs. Note that the first three members of this group are *not* outstanding in terms of their C/O or He/H abundances. All of our objects were chosen so as to have near-solar metallicities, and the range of that parameter among them is rather small. Thus, the lack of a metallicity trend among them in either C/O or N/O is not surprising. However, even with the extension of the sampled metallicity range provided especially by the LMC and SMC objects, the model-predicted trend remains elusive. This is perhaps due to the large amount of scatter observed among objects of similar metallicity (see below).

Three of our eight objects (IC 2165, NGC 7662, and PB6) show C/O ratios that are greater than or equal to the solar value. In the cases of IC 2165 and PB6 the C/O ratio exceeds unity, suggesting that their progenitor AGB stars experienced significant third dredge-up during which fresh carbon produced by triple-alpha processing was brought up by convection into the stellar atmosphere from the He-burning shell located just above the C-O core of the remnant star.

The left panels in Figure 7 show the distribution of our program objects and the KH database objects in the log(C/O) and log(N/O)-He/H planes. Note the suggestion of a positive correlation between log(N/O) and He/H. This has been noticed many times before; one such example is included in the extensive review by Kaler (1985). This positive behavior is predicted by stellar evolution models (see Marigo 2001; Karakas 2010) and is fundamentally associated with a positive correlation between N/O and stellar mass. In a follow-up paper to this one we explore more closely the relation between the progenitor masses and the abundance results of the present work.

Peimbert & Torres-Peimbert (1983) referred to those PNs in which He/H $\geqslant$ 0.125 and log(N/O) $\geqslant$ −0.30 as Type I objects, while PNs below these boundaries were considered to be non-Type Is. By these criteria then, NGC 2440 and PB6 are Type I objects, while the other six are non-Type Is. PB6's Type I membership is confirmed by Peña et al. (1998), who find He/H = 0.17 and log(N/O) = 0.14.

The PNs with supersolar N/O have several other interesting properties that distinguish them from those PNs with solar or subsolar N/O. The most dramatic are their morphologies. Members of the latter group are all elliptical in outline with very conspicuous central cavities surrounded by thin bright rims and smooth and sharply bounded shells. None of the PNs with supersolar N/O have similar morphologies. Either they are bipolar (NGC 2440), clumpy (PB6), or elliptical with central cavities but no thin rim (IC 2165 and NGC 5315). NGC 5315 is also a serendipitously discovered diffuse X-ray source (Kastner et al. 2008). Thin rims are the result of relatively gentle expansions of the hot cavities within them, whereas fractured rims are the result of instabilities induced by rapid cavity expansion at high pressure (Toalá & Arthur 2014). We note that as a rule, the nebular expansion velocities of PNs with [WC] nuclei are well above average (Górny & Stasińska 1995), again suggesting a high degree of momentum transfer from stellar winds during their evolutions.

The central stars of PNs with supersolar N/O also stand out from the others. NGC 5315 and PB6 have early-type WC or WO nuclei (see Kaler et al. 1991; Peña et al. 1998; Acker & Neiner 2003). The central star of NGC 2440 is the hottest known (Heap & Hintzen 1990). NGC 5315 and NGC 2440 have probably evolved from relatively massive progenitors whose mass-loss rates in radiation-driven winds are or have been very strong. The central star of IC 2165, whose progenitor is probably not as massive as these, may simply be at a high-temperature stage in its evolution.

Finally, an obvious characteristic in each of the four panels in Figure 7 is the large amount of point-to-point scatter in C/O, N/O, and He/H; scatter is present in all of the individual samples included in the figures. The sizes of the uncertainties (not indicated here to avoid visual confusion, but see Table 8) are dwarfed by the sizable scatter exhibited in each panel. Therefore, the scatter is very likely real and indicative of the wide range of chemical inhomogeneity in the ISM from which these stars formed at various places and times within the galaxy and/or in the amount of atmospheric self-pollution that AGB stars experience during the final evolutionary stages of these stars.

5. CONCLUSIONS

The STIS long-slit data from this program are the first co-spatial spectra of extended Galactic PNs that span the UV and optical bands at sub-arcsecond spatial resolution. These new data enable a detailed and consistent analysis of abundance and physical properties of PNs using both UV and optical emission lines from identically sampled volumes. Compared to prior abundance analyses of past decades that studied only the major optical emission lines, or that used satellite UV with ground-based data from different nebular regions, this work offers new insights on UV–optical emission variations and permits corresponding analysis of nebular diagnostics in C and N lines from their major ions. This initial study of these STIS data touches only the top of the science inherent in the data, which will be analyzed in more detail in future papers. These *HST* data are now in the public domain and offer future investigators a new and, perhaps, historical insight into the spatial variations of UV–optical emission for modeling physical diagnostics across the extent of photoionized nebulae.

We conclude that the central stars and the morphological outcomes of nebular evolution of PNs with super-solar N/O are not typical of those of PNs with solar N/O. Although the evidence is somewhat circumstantial in this paper, there is every reason to suppose that the central stars of PNs with super-solar N/O have evolved from some of the most massive stars that are able to form PNs. This is one of the reasons that we selected a PN sample with a wide range of N/O at constant O/H. It is therefore peculiar that PNs with super-solar N/O show no signs of C/O anomalies. Perhaps this can be explained by the conversion of C to N during HBB, thereby increasing the N while holding C to a level close to its original one in the progenitor star. On the other hand, the abundance trends in our graphs plotted against He/H indicate that selecting PN samples based on He enrichment will be a fruitful approach to understanding CNO production.

Finally, the amounts of scatter in the N/O and C/O ratios at roughly constant metallicity are much larger than can be explained by observational uncertainties (although we cannot rule out the possibility of systematic errors in earlier publications because of, e.g., mis-matched apertures between spectra from multiple wavelength regimes). In fact, the size of the scatter in our plot of C/O or N/O versus O/H dwarfs that observed among objects such as H II regions or main-sequence stars, regardless of metallicity. We surmise that this situation may reflect the self-polluting nature of objects in the AGB stage of evolution or the chemical history of the Galactic ISM at the time and place when the stars formed (Matteucci 2003).

Support for Program number GO–12600 was provided by NASA through a grant from the Space Telescope Science Institute, which is operated by the Association of Universities for Research in Astronomy, Incorporated, under NASA contract NAS5-26555. B.B. received partial support from NSF grant AST-0808201.

REFERENCES

Acker, A., & Neiner, C. 2003, A&A, 403, 659
Asplund, M., Grevesse, N., Sauval, A. J., & Scott, P. 2009, ARA&A, 47, 481
Bernard-Salas, J., Pottasch, S. R., Feibelman, W. A., & Wesselius, P. R. 2002, A&A, 387, 301
Biretta, J., et al. 2015, STIS Instrument Handbook (Version 14.0; Baltimore: STScI)

Bohigas, J., Rodríguez, M., & Dufour, R. J. 2013, RMxAA, 49, 227
Bostroem, K., & Proffitt, C. (ed.) 2011, STIS Data Handbook (Version 6.0; Baltimore: STScI)
Corradi, R. L. M., Goncalves, D. R., Villaver, E., et al. 2000, ApJ, 535, 3
Corradi, R. L. M., Schönberner, D., Steffen, M., & Perinotto, M. 2003, MNRAS, 340, 417
Dufour, R. J. 1991, PASP, 103, 857
Esteban, C., Peimbert, M., García-Rojas, J., et al. 2004, MNRAS, 355, 229
Fang, X., Guerrero, M. A., Marquez-Lugo, R. A., et al. 2014, ApJ, 797, 100
García-Rojas, J., Peña, M., & Peimbert, A. 2009, A&A, 496, 139 (GRPP)
Górny, S. K., & Stasińska, G. 1995, A&A, 303, 893
Heap, S. R., & Hintzen, P. 1990, ApJ, 353, 200H
Henry, R. B. C., Kwitter, K. B., & Bates, J. A. 2000, AJ, 531, 928
Henry, R. B. C., Kwitter, K. B., & Balick, B. 2004, AJ, 127, 2284
Henry, R. B. C., Kwitter, K. B., & Howard, J. W. 1996, ApJ, 458, 215
Holland, S. T., Alessandra, A., Bostroem, A., Oliveira, C., & Proffitt, C. 2014, Instrument Science Rep. STIS 2014-02 (Baltimore: STScI)
Hyung, S. 1994, ApJS, 90, 119
Johnson, M. D., Levitt, J. S., Henry, R. B. C., & Kwitter, K. B. 2006, in IAU Symp. 234, ed. M. J. Barlow, & R. Méndez (Cambridge: Cambridge Univ. Press), 439
Kaler, J. B. 1985, ARA&A, 23, 89
Kaler, J. B. 1986, ApJ, 308, 322
Kaler, J. B., Shaw, R. A., Feibelman, W. A., & Imhoff, C. L. 1991, PASP, 103, 67
Karakas, A. I. 2010, MNRAS, 403, 1413
Kastner, J. H., Montez, R., Jr, Balick, B., & de Marco, O. 2008, ApJ, 672, 957
Keller, G. R., Bianchi, L., & Maciel, W. J. 2014, MNRAS, 442, 1379
Kingsburgh, R. L., & Barlow, M. J. 1994, MNRAS, 271, 257
Koeppen, J., & Aller, L. H. 1987, in Exploring the Universe with the IUE Satellite (Dordrecht: Reidel), 589
Krabbe, A. C., & Copetti, M. V. F. 2006, A&A, 450, 159
Kwitter, K. B., & Henry, R. B. C. 1996, ApJ, 473, 304
Kwitter, K. B., & Henry, R. B. C. 1998, ApJ, 493, 247
Kwitter, K. B., & Henry, R. B. C. 2001, ApJ, 562, 804
Kwitter, K. B., Henry, R. B. C., & Milingo, J. B. 2003, PASP, 115, 80
Liu, X.-W., Barlow, M. J., Zhang, Y., Bastin, R. J., & Storey, P. J. 2006, MNRAS, 368, 1959
Liu, Y., Liu, X.-W., Barlow, M. J., & Luo, S.-G. 2004, MNRAS, 353, 1251
Liu, Y., Liu, X.-W., Luo, S.-G., & Barlow, M. J. 2004, MNRAS, 353, 1231
Marigo, P. 2001, A&A, 370, 194
Matteucci, F. 2003, Ap&SS, 284, 539
Milingo, J. B., Henry, R. B. C., & Kwitter, K. B. 2002, ApJS, 138, 285
Milingo, J. B., Kwitter, K. B., Henry, R. B. C., & Souza, S. P. 2010, ApJ, 711, 619
Peimbert, M., & Torres-Peimbert, S. 1983, in IAU Symp. 103, Planetary Nebulae (Dordrecht: Reidel), 233
Peña, M., Stasińska, G., Esteban, C., et al. 1998, A&A, 337, 866
Perinotto, M. 1991, ApJS, 76, 687
Pottasch, S. R., Beintema, D. A., Bernard-Salas, J., Koornneef, J., & Feibelman, W. A. 2002, A&A, 393, 285
Pottasch, S. R., & Bernard-Salas, J. 2008, A&A, 490, 715
Pottasch, S. R., Bernard-Salas, J., Beintema, D. A., & Feibelman, W. A. 2004, A&A, 423, 593
Rola, C., & Stasińska, G. 1994, A&A, 282, 199
Savage, B. D., & Mathis, J. S. 1979, ARA&A, 17, 73
Seaton, M. J. 1979, MNRAS, 187, 73P
Shaw, R. A., Lee, T.-H., Stanghellini, L., et al. 2010, ApJ, 717, 562
Stanghellini, L., Lee, T.-H., Shaw, R. A., Balick, B., & Villaver, E. 2009, ApJ, 702, 733
Stanghellini, L., Shaw, R. A., & Gilmore, D. 2005, ApJ, 622, 294
Stasińska, G., Richer, M. G., & McCall, M. L. 1998, A&A, 336, 667
Toalá, J. A., & Arthur, S. J. 2014, MNRAS, 443, 3486
Tsamis, Y. G., Barlow, M. J., Liu, X.-W., Danziger, I. J., & Storey, P. J. 2003, MNRAS, 345, 186